Aerosol model evaluation using two geostationary satellites over East Asia in May 2016

Goto, Daisuke
National Institute for Environmental Studies (NIES)

Kikuchi, Maki
Earth Observation Research Center (EORC), Japan Aerospace Exploration Agency (JAXA)

Suzuki, Kentaroh
Atmosphere and Ocean Research Institute, University of Tokyo

Hayasaki, Masamitsu
Japan Automobile Research Institute

他

出版情報：Atmospheric Research. 217, pp.93-113, 2019-03-01. Elsevier
バージョン：

Atmospheric Research 217 (2019) 93–113

Contents lists available at ScienceDirect

Atmospheric Research

journal homepage: www.elsevier.com/locate/atmosres

Aerosol model evaluation using two geostationary satellites over East Asia in May 2016

Daisuke Goto[a,*], Maki Kikuchi[b], Kentaroh Suzuki[c], Masamitsu Hayasaki[d], Mayumi Yoshida[b], Takashi M. Nagao[b], Myungje Choi[e], Jhoon Kim[e], Nobuo Sugimoto[a], Atsushi Shimizu[a], Eiji Oikawa[f], Teruyuki Nakajima[b]

[a] National Institute for Environmental Studies (NIES), 16-2 Onogawa, Tsukuba, Ibaraki 305-8506, Japan
[b] Earth Observation Research Center (EORC), Japan Aerospace Exploration Agency (JAXA), Japan
[c] Atmosphere and Ocean Research Institute, University of Tokyo, Japan
[d] Japan Automobile Research Institute, Japan
[e] Department of Atmospheric Sciences, Yonsei University, Republic of Korea
[f] Research Institute for Applied Mechanics, Kyushu University, Japan

ARTICLE INFO

Keywords:
Aerosols
Geostationary satellite
Siberian wildfire
Model evaluation

ABSTRACT

This study newly applies measurements from two geostationary satellites, the Advanced Himawari Imager (AHI) onboard the geostationary satellite Himawari-8 and the Geostationary Ocean Color imager (GOCI) onboard the geostationary satellite COMS, to evaluate a unique regional aerosol-transport model coupled to a non-hydrostatic icosahedral atmospheric model (NICAM) at a high resolution without any nesting technique and boundary conditions of the aerosols. Taking advantage of the unique capability of these geostationary satellites to measure aerosols with unprecedentedly high temporal resolution, we focus on a target area (115°E-155°E, 20°N-50°N) in East Asia in May 2016, which featured the periodic transport of industrial aerosols and a very heavy aerosol plume from Siberian wildfires. The aerosol optical thickness (AOT) fields are compared among the AHI, GOCI, MODIS, AERONET and NICAM data. The results show that both AHI- and GOCI-retrieved AOTs were generally comparable to the AERONET-retrieved ones, with high correlation coefficients of approximately 0.7 in May 2016. They also show that NICAM successfully captured the detailed horizontal distribution of AOT transported from Siberia to Japan on the most polluted day (18 May 2016). The monthly statistical metrics, including correlation between the model and either AHI or GOCI, are estimated to be > 0.4 in 42–49% of the target area. With the aid of sensitivity model experiments with and without Siberian wildfires, it was found that a long-range transport of aerosols from Siberian wildfires (from as far as 3000 km) to Japan influenced the monthly mean aerosol levels, accounting for 7–35% of the AOT, 26–49% of the surface PM2.5 concentrations, and 25–66% of the aerosol extinction above 3 km in height over Japan. Therefore, the air pollutants from Siberian wildfire cannot be ignored for the spring over Japan.

1. Introduction

Understanding the spatial structure of air pollution in East Asia, which is one of the most polluted areas in the world, is essential to address environmental issues and their effects on human health. Air pollution measurements are a useful tool to monitor air quality and have been continually conducted at observation sites. During the 2000s, remote-sensing methods such as Aerosol Robotic Network (AERONET) (Holben et al., 1998) and light detection and ranging (LIDAR) networks (Sugimoto et al., 2008) were developed to conduct such measurements. Polar-orbiting satellites with remote-sensing sensors were also launched to measure air pollution, including the Moderate Resolution Imaging Spectroradiometer (MODIS) onboard the Terra and Aqua satellites (https://modis.gsfc.nasa.gov/). Recently, the Atmospheric Environmental Regional Observation System (AEROS), including > 500 sites in Japan, was installed to monitor PM2.5 mass concentrations and has provided prompt reports that are regularly released through Japan's Ministry of the Environment (http://soramame.taiki.go.jp/).

However, the coverage area and temporal resolution of these systems are inadequate for precisely capturing air pollutants, which vary

* Corresponding author.
E-mail address: goto.daisuke@nies.go.jp (D. Goto).

https://doi.org/10.1016/j.atmosres.2018.10.016
Received 17 August 2018; Received in revised form 23 October 2018; Accepted 23 October 2018
Available online 02 November 2018

temporally and spatially within a short atmospheric lifetime. For example, instruments that collect in situ measurements have been employed at many sites, but the number of observation sites is limited to land, and air pollution data are generally limited to near the surface. LIDAR can obtain vertical air-pollution information with high temporal resolution but suffers from cloud contamination and a limited number of sites. A MODIS sensor onboard the polar-orbiting satellites can retrieve information such as aerosol optical properties with moderate accuracy and wide observational coverage on a global scale. However, these satellites have highly restricted sampling rates, i.e., once per day and only under clear-sky and ice/snow-free conditions. Therefore, the measurements alone cannot fully capture the 4-dimensional structure of air pollution.

Recently, two geostationary satellites that can be used to monitor air pollution were launched over East Asia. One is the Korean Geostationary Ocean Color Imager (GOCI) onboard the Communication, Ocean, and Meteorological Satellite (COMS) (Choi et al., 2012). The GOCI can measure aerosol optical properties such as the aerosol optical thickness (AOT) over East Asia by using multiple wavelengths (Lee et al., 2010). The GOCI-retrieved AOT from March 2011 was estimated over East Asia (116°E–146°E, 24°N–48°N) with a horizontally and temporally high resolution (Choi et al., 2018). The other geostationary satellite is the Japanese geostationary satellite Himawari-8, which carries the multispectral imaging sensor known as the Advanced Himawari Imager (AHI) and was launched in October 2014. The AHI-retrieved AOT also has high horizontal and temporal resolution and is available since official operation began in July 2015 (Yoshida et al., 2018; Kikuchi et al., 2018). Both geostationary satellites can measure radiative signals at visible wavelengths with a much higher temporal resolution than that of polar-orbiting satellites. In this study, we analyze the AHI- and GOCI-retrieved AOTs along with ground-based measurements to better understand the 4-dimensional structure of air pollution in East Asia.

In addition to these measurements, atmospheric transport models can be applied to better characterize the 4-dimensional behavior of air pollution. In this study, we use a semi-regional aerosol-transport model (Goto et al., 2015a), i.e., the non-hydrostatic icosahedral atmospheric model (NICAM) (Tomita and Satoh, 2004; Satoh et al., 2008, 2014), alongside aerosol components (Takemura et al., 2005; Suzuki et al., 2008) and a stretched grid system (Tomita, 2008a). The simulated aerosol distributions have previously been evaluated by using multiple measurements of in situ sampling and LIDAR data (Goto et al., 2015a). Goto et al. (2015a) validated simulated aerosol distributions from August 2007 around Japan by using measurements of the surface PM2.5 that were obtained via AEROS and the vertical profiles of the observed aerosols at two sites that were operated by a network of NIES-LIDAR systems (Sugimoto et al., 2008). Goto et al. (2015a) found that this model could simulate aerosols with diurnal and synoptic variations during the summer around Japan. Goto et al. (2016) also applied this model to present and future scenario experiments over Japan during the entire year. The unique capability of NICAM with the stretched grid system is that it does not need nesting and boundary conditions, which are used in a usual regional transport model (Morino et al., 2015). This point can be an advantage to simulate long-range transport of aerosols, because NICAM with the stretched grid system can eliminate numerical noise caused by the boundary.

Transboundary pollution in East Asia is greatest during the spring and has been investigated in previous field campaigns (e.g., Seinfeld et al., 2004; Nakajima et al., 2007). During this season, air pollution, including anthropogenic emissions and dust particles, is constantly transported from the continent to the oceans and Japan. In addition, Siberian wildfires regularly occur, and the emitted aerosols are sometimes transported to Japan. Ikeda and Tanimoto (2015) showed that Siberian wildfire events in 2003 and 2008 strongly affected the surface PM2.5 concentrations in northern Japan by using a chemistry transport model. Yasunari et al. (2018) demonstrated that Siberian wildfires sometimes provided a high concentration of the surface PM2.5 i in Hokkaido, northern Japan, when snow melts earlier, as well as large-scale wildfires that occur over eastern Eurasia in spring to summer. Although such transboundary pollution from other regions should be monitored to track air pollution in response to societal demands, such air pollution, including biomass burning and its 4-dimensional structure, have not yet been fully understood. Therefore, we analyze May 2016, which is the spring season in Japan, using the stretched grid NICAM and multiple measurements, including those from two instruments onboard different geostationary satellites, AHI and GOCI; the MODIS instrument onboard two polar-orbiting satellites, Terra and Aqua; and ground-based measurements datasets made using AERONET, LIDAR and in situ sampling of PM2.5.

To evaluate the spatiotemporal variability of NICAM-simulated aerosols over Japan in the case of May 2016, we first estimate the accuracies of two geostationary satellites using independent measurements of AERONET. These geostationary satellites can provide greater temporal resolution than polar-orbiting satellites. After demonstrating the availability of two geostationary satellites as reference datasets, we then investigate the differences in the AOT as shown by AHI, GOCI, and NICAM. A description of the model and measurements used in this study is provided in Sections 2 and 3. After comparing the NICAM-simulated AOT to both the AHI-retrieved and GOCI-retrieved AOTs in Section 4, we discuss how well the model simulates transboundary pollution, including the Siberian biomass burning, captured by the four measured datasets, i.e., AHI, GOCI, AEROS and LIDAR, during May 2016 (Section 4.4). In Section 4.4, we investigate the relationship of aerosols among the following: the column amount, the surface concentration and the vertical profile on each event. We also discuss the effect of the Siberian biomass burning that occurred in May 2016 on the aerosol levels around Japan by conducting a sensitivity test for Siberian wildfires with the NICAM. We summarize our findings in Section 5. The unique contribution of this study lies in its position as the first study to evaluate air pollution using multiple payloads onboard the so-called next-generation geostationary satellites.

2. Model description and experimental design

NICAM is a non-hydrostatic icosahedral atmospheric model and is usually used as a global model with a uniform grid system (Tomita and Satoh, 2004; Satoh et al., 2008, 2014). NICAM also implements a stretched grid system, which allows NICAM to run at a high resolution over a specific area with relatively light computer-resource demands (Tomita, 2008a). The stretched grid has been applied to the regional simulation of clouds (Satoh et al., 2010; Seiki et al., 2014) and air pollutants (Goto et al., 2015a, 2016, 2018; Trieu et al., 2017). In this study, we run NICAM with an identical framework, i.e., a dynamic core, physical processes, spatial resolution and time steps, to that in Goto et al. (2015a). The stretched grid center is set at the point (140.0°E, 35.0°N). The finest grid spacing is 11 km around the center. The grid spacing increases far from the center. For example, the grid spacing is approximately 25 km over Japan and approximately 40 km around Beijing. The number of vertical layers is 38, including 12 layers below 3 km in height. The time steps are set at 30 s. The cloud microphysics module is NSW6 (Tomita, 2008b) without any cumulus parameterization according to previous studies (Tomita et al., 2005; Sato et al., 2009). The vertical turbulent mixing is Level 2 of the MYNN scheme (Mellor and Yamada, 1974; Nakanishi and Niino, 2004). The differences from the experimental design of Goto et al. (2015a) are the following three points: the target period, the emission inventory of the biomass burning, and the aerosol module for wet deposition. The start time of the model integration is set at 1 April 2016, and the analysis period is 1–30 May 2016. The distribution of the daily sea surface temperature (SST) and the 6-hourly air temperature and wind values are obtained by using the NCEP-FNL reanalysis data (NCEP, 2000). The 6-hourly meteorological fields are nudged above a 2 km height in this

experiment, as in our previous studies (Goto et al., 2015a, 2016; Trieu et al., 2017). The inventory of the daily biomass burning is taken from the Global Fire Assimilation System (GFAS) version 1.2 (Kaiser et al., 2012).

The aerosol module is based on SPRINTARS (Takemura et al., 2005; Goto et al., 2015a). This module considers 4 different aerosol species: carbonaceous aerosols, sulfate, dust and sea salt. The carbonaceous aerosols comprise black carbon (BC) and organic carbon (OC). The OC in SPRINTARS considers primary and biogenic secondary components. These aerosols are subjected to various atmospheric processes, such as transport, vertical diffusion, chemical formation, wet and dry deposition, and gravitational settling. The physical, chemical, and optical properties of the aerosols considered in this module are identical to those in our previous studies (Goto et al., 2015a; Dai et al., 2014). The AOT is evaluated at the wavelength of 0.55 μm. The PM2.5 components of this study are defined as the sum of the BC; the anthropogenic OC multiplied by 1.6, which is then called organic matter (OM); the biomass burning OC multiplied by 2.6 as OM; the sulfate and assumed ammonium, which are together derived by multiplying the sulfate by 1.27 and are called ammonium sulfate; and the smaller bins of sea salt and dust.

The SPRINTARS module was originally developed for climate research with a low horizontal resolution from 100 to 300 km (e.g., Takemura et al., 2005). Recently, this module was applied to a regional simulation with a high horizontal resolution of approximately 10 km (Goto et al., 2015a). In Goto et al. (2015a), the cloud fraction in the model is set to 1, even when only tiny clouds with very weak precipitation are present in the model grid, since the cloud microphysics module of NSW6 (Tomita, 2008b) in the high-resolution model does not calculate the cloud fraction of the model grid. In this study, however, the cloud fraction is set to 0, such that the liquid water content is $< 1 \times 10^{-5}$ (kg kg^{-1}), which is the detection limit of the satellite measurements. This modification can strengthen the consistency of the processes between aerosols, clouds and precipitation and can improve the overestimation of the wet deposition of the aerosols by very weak precipitation fluxes, although this did not provide improved results for the target area and period in this study.

The model in this study was evaluated by using statistical metrics: the mean, correlation coefficient (R), normalized mean bias (NMB), and root-mean-square error (RMSE). These two parameters (the mean and correlation coefficient) are often used in model evaluation. In this study, NMB and RMSE are defined as follows:

$$NMB = \frac{1}{N} \times \frac{\sum_{i=1}^{N} (\tau_{\mathrm{NICAM(i)}} - \tau_{\mathrm{obs(i)}})}{\sum_{i=1}^{N} \tau_{obs(i)}} \times 100\ [\%] \quad (1)$$

$$RMSE = \sqrt{\frac{\sum_{i=1}^{N} (\tau_{\mathrm{NICAM(i)}} - \tau_{\mathrm{obs(i)}})^2}{N}} \quad (2)$$

where $\tau_{\mathrm{NICAM(i)}}$ and $\tau_{\mathrm{obs(i)}}$ are one-hourly datasets for the NICAM-simulated AOT and the observed or retrieved AOT, respectively. N is the sampling number. The following two parameters to quantify the statistical metrics and express the probability distribution function (PDF) are also defined:

$$\mathrm{Skewness} = \frac{1}{\mathrm{N}} \times \frac{\sum_{\mathrm{i=1}}^{\mathrm{N}} (\tau_{\mathrm{i}} - \tau_{\mathrm{ave}})^3}{\sigma^3}, \quad (3)$$

$$\mathrm{Kurtosis} = \frac{1}{\mathrm{N}} \times \frac{\sum_{\mathrm{i=1}}^{\mathrm{N}} (\tau_{\mathrm{i}} - \tau_{\mathrm{ave}})^4}{\sigma^4}, \quad (4)$$

where τ_{i} and τ_{ave} are one-hourly datasets for the AOT and monthly mean AOT, respectively. The sigma value represents one standard deviation of the PDF. N is the sampling number. The skewness is 0 if the PDF is a normal distribution and positive if the AOT in the critical value is smaller than the mean AOT. The kurtosis represents the difference between maximum and minimum values of the profile in the PDF. A large kurtosis value represents a sharp feature in the PDF.

To identify the impacts of Siberian biomass burning on the total aerosol amount, we conducted two sensitivity tests: an experiment without all biomass-burning emissions and an experiment without Siberian biomass-burning emissions. The Siberian region is defined as a rectangular area (90.0°E–140.0°E, 50.0°N–60.0°N). The results of the sensitivity tests are used in the analysis of the aerosol sources and the effect of the Siberian biomass burning in Section 4.

3. Data description

3.1. AHI

The AHI on board Himawari-8 began official operation in July 2015. The AHI has 16 observation bands, including 3 visible (0.46, 0.51, and 0.64 μm), 3 near-infrared (0.86, 1.6 and 2.3 μm), and 10 infrared (from 3.9 to 13.3 μm) bands. The number of bands in the AHI is greater than that of the previous sensors onboard Himawari-6 and -7. The aerosol optical properties are retrieved by an algorithm that uses 5 wavelengths over land (0.46, 0.51, 0.64, 0.86 and 1.6 μm) and an algorithm that uses 2 near-infrared wavelengths over the ocean (0.86 and 1.6 μm) (Higurashi and Nakajima, 2002; Fukuda et al., 2013; Yoshida et al., 2018). The single-scattering albedo at 0.5 μm and the Ångström exponent at 0.4 and 0.6 μm are also retrieved by using the method of Yoshida et al. (2018), which can be applied to multiple satellites.

Although aerosol optical products were originally observed every 10 min by the AHI/Himawari (Yoshida et al., 2018), hourly products were developed for Himawari-8 to minimize the number of cloud-contaminated pixels; these products rely on optimal interpolation to 1 h of the original 10-min product (Kikuchi et al., 2018). These products were well validated by Yoshida et al. (2018) and Kikuchi et al. (2018). The mean bias and RMSE of the level 3 AOT product between independent AERONET observation and AHI were calculated to be +0.013 and 0.095, respectively (Yoshida et al., 2018). The aerosol datasets are available from the JAXA Himawari Monitor website (http://www.eorc.jaxa.jp/ptree/index.html).

In this study, the AOT at the 0.51 μm wavelength in version 2.0 is used for model evaluation. The original data were released by the Earth Observation Research Center (EORC) of the Japan Aerospace Exploration Agency (JAXA) using the square of the lattice of 0.05°, but the AHI-retrieved values were averaged over the square of the lattice of 0.2° for comparison with the model results. The lattice of 0.2° includes 16 pixels of the original dataset, so these values are averaged by using > 8 pixels in the lattice. Conversely, lattices with fewer than 9 pixels are undefined.

3.2. GOCI

The GOCI on board COMS began its official operation in March 2011. The target area of GOCI is East Asia, covering a 2500 km × 2500 km area centered at 130°E, 36°N, which includes the Eastern China, Korea, and Japan. The GOCI has 8 observation bands, including 6 visible (0.412, 0.443, 0.490, 0.555, 0.660, and 0.680 μm) and 2 near-infrared (0.745 and 0.865 μm) bands. The GOCI aerosol optical properties are retrieved by a land algorithm that uses the wavelengths where surface reflectance is < 0.15, a dark ocean algorithm that uses four wavelengths, i.e., 0.412, 0.443, 0.765, and 0.865 μm, and a turbid ocean algorithm that uses two wavelengths, i.e., 0.412 and 0.865 μm, which are based on the GOCI Yonsei aerosol retrieval version 2 algorithm (Choi et al., 2018). A total of 12 × 12 pixels of original 500 m GOCI radiance data are aggregated to one 6 km × 6 km pixel for aerosol products to increase the aerosol signal after cloud masking. The temporal resolution of GOCI is 1 h from 00:30 to 07:30 UTC. The detailed aerosol retrieval algorithm and validation results are described in Choi et al. (2016, 2018). The AOT at 0.55 μm is a main retrieval product, and the Ångström exponent between 0.44 and 0.87 μm, the fine-

mode fraction at 0.55 μm, and single-scattering albedo at 0.44 μm are ancillary retrieval products. The accuracy is ± (0.073 + 0.137*AOT) over land and ± (0.037 + 0.185*AOT) over ocean, where AOT is the AERONET-retrieved one (Choi et al., 2018). The GOCI Level 1B radiance data are released by the Korea Ocean Satellite Center (KOSC) at the Korean Institute of Ocean Science and Technology (KIOST) website (http://kosc.kiost.ac.kr/), and the GOCI aerosol data will be available at the same website.

In this study, the grids are converted into the lattice of 0.2°, similar to that of AHI. It means that the AOT in the lattice of 0.2° is defined only when > 50% of pixels of the total lattice of 0.2° are defined. The GOCI aerosol products are currently available from the authors at Yonsei University.

3.3. MODIS

MODIS is a sensor on board the polar-orbiting satellites Terra and Aqua and is designed to observe optical properties of both aerosols and clouds with 36 bands at a global scale (Kaufman et al., 1997). The AOT retrieved from MODIS is often used as reference data for model evaluation (Kinne et al., 2003). The MODIS/Terra retrieved AOT is available from 2000 and MODIS/Aqua-retrieved AOT is from 2002. The MODIS/Terra measures on local time 10:30 and the MODIS/Aqua does on local time 13:30. One of the retrieval methods of MODIS/Terra and MODIS/Aqua is a deep blue method (Hsu et al., 2013) and a dark target method (Levy et al., 2013) over land and the dark target over oceans (Sayer et al., 2014).

In this study, we use both the deep blue and dark target results in Level 2 of Collection 6. We also converted the original grids to the lattice of 0.2°. We use both MODIS/Terra and MODIS/Aqua, so at most two-sampling data of AOT in one day can be used for the model evaluation. The uncertainty of retrieved AOT by the dark target method is ± (0.05 + 0.15*AOT) in a global scale, where AOT is the AERONET-retrieved one (e.g., Levy et al., 2013). In the deep blue method, the uncertainty of the retrieved AOT is almost comparable to that obtained by the dark target method under the typical aerosol levels (AOT is 0.1 to 0.5) (Sayer et al., 2014).

3.4. AERONET

The AERONET is the most reliable to observe the aerosol optical properties from the ground (Holben et al., 1998). The use of the AERONET as a reference dataset is currently the most common way. The measurement starts from 1998 to the present. The number of the available sites is increasing. In our target region and period, almost 50 sites are operational, but at some sites the number of the available datasets is limited. Additionally, during the period of May 2016 in East Asia under the DRAGON campaign to capture aerosol optical properties, some sites were very nearly located at each other (Holben et al., 2018). Therefore, in this study, we actually use the 19 AERONET sites, which are located at least 0.2° distance, for the evaluation of model as well as the two geostationary satellites in Section 3.7 and 15 AERONET sites, which are located at least 1° distance, for a comparison of the temporal variation in Section 4.1. The temporal resolution is 10 min in the original dataset, so we also temporally average them over 1 h. We focus on the visible wavelength of AOT, i.e., 0.5 μm, for the evaluation and comparison. The accuracy of level 2 AOT at 0.5 μm is approximately 0.01 (Holben et al., 1998). The AERONET dataset is version 3.

3.5. PM2.5 measurements

Operational PM2.5 measurements were utilized in this study for model evaluation. In Japan, the operational system AEROS provides regular reports via the website of the Ministry of Japan (http://soramame.taiki.go.jp/). The PM2.5 are collected on polytetrafluoroethylene (PTEE) filter tapes and their hourly mass concentrations are automatically measured by the beta-ray attenuation method. These automatic measuring devices satisfy the Japanese Industrial Standard (JIS) Z 8851, which supports the standard measurement method of the Ministry of the Environment, such as quality control under low relative-humidity (RH) conditions. In this study, we focus on the following three areas: Fukuoka (130.0°E–131.0°E, 33.0°N–34.0°N), Kantou (138.5°E–141.0°E, 34.0°N–37.0°N), and Hokkaido (138.5°E–146.0°E, 41.5°N–46.0°N). The sites that are available for these areas vary from day to day but include 44 sites in Fukuoka, 262 sites in Kantou, and 19 sites in Hokkaido. The observed PM2.5 values within these areas are spatially averaged for model evaluation.

3.6. LIDAR

LIDAR data are available from the Asian dust and aerosol lidar observation network (AD-Net) to capture the vertical profiles of the aerosols (Sugimoto et al., 2008). The results are promptly posted on the website of the NIES in Japan (http://www-lidar.nies.go.jp/AD-Net/) (Sugimoto et al., 2003; Shimizu et al., 2004). The LIDAR network includes > 10 sites in Japan that can also be used for model validation. In this study, three sites are selected from different regions in Japan. These three sites are Fukuoka (130.5°E, 33.5°N), Tokyo (139.7°E, 35.7°N), and Niigata (138.9°E, 37.8°N). The Niigata site is the closest to Hokkaido (138.5°E–146.0°E, 41.5°N–46.0°N) of the available sites in the AD-Net in May 2016. The LIDAR system measures the backscattering intensity at 532 and 1064 nm and the depolarization ratio at 532 nm. By using these products, the vertical extinctions of the aerosols can be determined using a retrieval algorithm (Sugimoto et al., 2003; Shimizu et al., 2004). The datasets are often used in model validations (Hara et al., 2011; Goto et al., 2015a, 2015b). In this study, we compare LIDAR-retrieved extinctions for spherical particles with the model-simulated results because we focus on transboundary aerosol transport, including Siberian biomass burning from the East Asian continent to the outflow regions in May, when fine particles are often the main contributors to the total atmospheric pollution.

3.7. Accuracy of AOT between AHI, GOCI, MODIS, and AERONET

This study applied multiple geostationary satellites, AHI/Himawari and GOCI/COMS. The GOCI-retrieved AOTs have been adequately evaluated using independent measurements including AERONET and MODIS in previous papers (e.g., Choi et al., 2016, 2018). However, the coverage area of GOCI-retrieved AOT is limited to a part of East Asia. In contrast, AHI/Himawari can cover larger areas including the whole of East Asia and Siberia. The AHI-retrieved AOTs started to be evaluated using the independent measurements (Yoshida et al., 2018), but the validation may still be limited. Furthermore, the retrieval technique in AHI is different from that in GOCI, because the observed wavelengths in two sensors (AHI and GOCI) are different. GOCI has a sensor in the ultraviolet wavelength, which is preferred when retrieving AOT over land. AHI has multiple sensors in the visible wavelength, which helps to accurately retrieve AOT at the visible wavelength. Therefore, it is not immediately obvious which geostationary satellite-retrieved AOT is better. In this study, the differences in AOT between the two satellites over the overlapping areas where both AHI and GOCI retrieve AOT are assumed as to be the uncertainty in the retrieved AOT.

Before the model evaluation, the satellite-retrieved aerosol products were evaluated by an independent dataset, AERONET, in May 2016 over East Asia. The spatially and temporally averaged AOTs from AHI, GOCI, and MODIS are compared at selected AERONET sites using statistical metrics: sampling number, correlation coefficient, NMB, and RMSE, as shown in Fig. 1. The compared sites of AERONET were selected when the sampling number of temporally collocated AOT between AERONET and AHI or between AERONET and GOCI was > 20. In the spatial criteria, the averaged lattice of 0.2° by 0.2° in AHI, GOCI, and MODIS, as explained in the previous sections, were selected at one

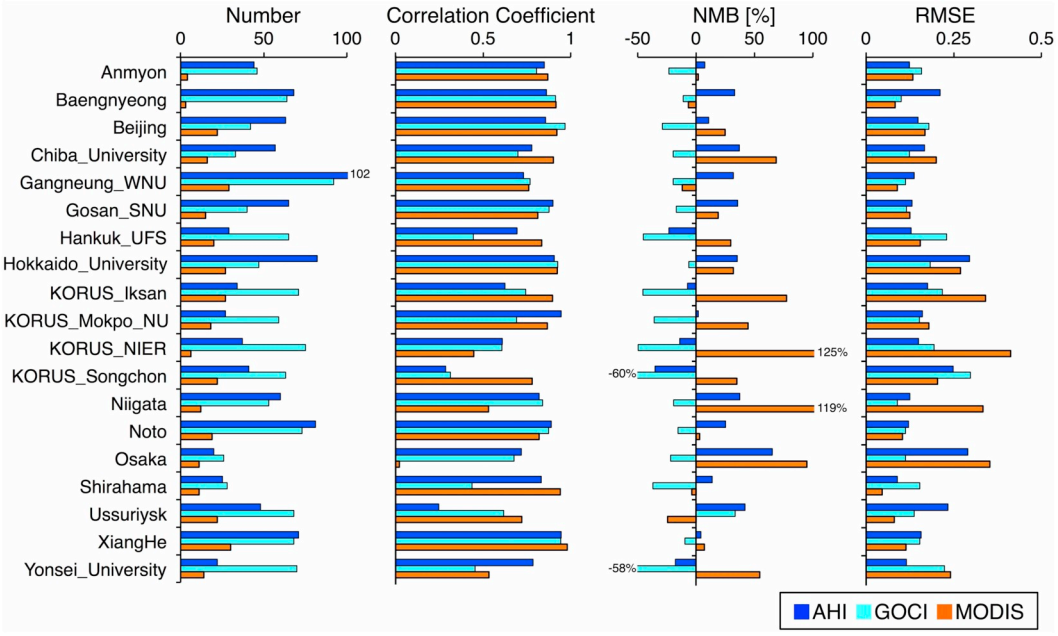

Fig. 1. Statistical metrics at 19 selected AERONET sites in May 2016.

lattice that included an AERONET site. Thus, this study assumes a smaller range of 0.2° by 0.2° as a representative grid at the site compared to other studies, such as Choi et al. (2018), which averaged satellite pixels within a 25 km radius from AERONET sites. In addition, this study assumes that the differences in the AOTs in the visible wavelength between 500 and 550 nm are negligible.

The sampling number varies on satellites, because of the limited number of temporal collocations among satellites and AERONET. The geostationary satellite instruments AHI and GOCI measure much more high-resolution temporal variations in aerosols than the polar-orbiting satellite instrument MODIS. The number in AHI and GOCI is in the range of < 100, whereas that in MODIS is < 30. It is caused by the missing retrieved AOT from AHI and GOCI due to the existence of clouds and retrieval error, especially over lands. The correlation coefficient between AHI and AERONET ranges from 0.61–0.95 (approximately 0.75 in 19 sites on average) except for two sites, KORUS_Songchon and Ussuriysk. The NMB ranges from −35% to +65% with an average of 0.15. The RMSE is 0.09–0.30 with an average of 0.17. At two exceptional sites, the NMB and RMSE are also larger. Especially at Ussuriysk, during the heavy air pollution during 18–22 May shown in Figs. 2 and 6, the AHI-retrieved AOT tends to be higher than the AERONET-retrieved AOT. Therefore, the overestimation during the heavy air pollution causes the low correlation coefficient. The correlation between GOCI and AERONET is also high, with the values of 0.44–0.97 (approximately 0.72 in 19 sites on average), except for KORUS_Songchon. The NMB values tend to be negative, but the RMSE is 0.09–0.30 with the average of 0.16. The RMSE values obtained from GOCI and AERONET are very similar to those from AHI and AERONET. The exception site, KORUS_Songchon, is located very near the other AERONET site, KORUS_Baeksa, within a distance of < 0.1° by 0.1°. At KORUS_Baeksa, the correlation coefficient is 0.62 (not shown in the figure, because this study eliminates some sites that are located too close to other sites). Therefore, the results at KORUS_Songchon may be very localized. Although the sampling number is very limited, the correlation between MODIS and AERONET is estimated to be high, with a correlation coefficient of 0.45–0.98 (approximately 0.76 in 19 sites on average) except for Osaka. The NMB and RMSE are calculated to be from −24% to +125% (with an average of 36%) and from 0.05 to 0.41 (with an average of 0.19). The bias between MODIS and AERONET tends to be larger than that between the two geostationary satellites and AERONET. The correlation coefficients between the satellites and AERONET are generally high to moderate; thus, the satellite results can be used as reference data for model evaluation.

The NICAM evaluation is conducted in Section 4. Without any measurements, NICAM results can be a piece of information about the aerosol distribution.

4. Results and discussion

4.1. Case study on 18 May 2016

During May 2016, Siberian wildfires produced heavy air pollutants, especially on 18 May 2016 (e.g., Yumimoto et al., 2018). In this section, we evaluate NICAM-simulated AOT using multiple satellites on that day. The top panels in Fig. 2 illustrate the horizontal distributions of the AOT as retrieved by the AHI and GOCI and as simulated by NICAM at 00:00 UTC (09:00 JST) on 18 May 2016. At that time, the figures show that both the AHI and GOCI captured the high-AOT plume over the northern Sea of Japan. The figures also indicate fire spots with black-triangle marks. The fire spots can be detected around Lake Baikal in Siberia. However, the AHI, GOCI, and MODIS data could not be used to determine a clear source for the plume because both the satellite-retrieved AOTs were limited by the presence of clouds and high albedo over land and because only the GOCI cannot cover the fire spots due to the limitation of coverage area over East Asia. Over the Sea of Japan, NICAM successfully simulated AOTs that were comparable to those from the AHI and GOCI. Furthermore, the detailed horizontal distributions of the high AOTs that were simulated by NICAM were relatively consistent with those from the AHI and GOCI. NICAM clearly identified the high plume as biomass burning emissions that were transported from Siberia, especially near Lake Baikal.

Because the geostationary satellites collect high temporal resolution AOT information, the model could be evaluated during the full daytime period on 18 May. Fig. 2 illustrates the horizontal distribution of the AOT for every 1 or 2 hourly snapshot on 18 May, i.e., at 01:00 UTC, 03:00 UTC, 04:00 UTC and 06:00 UTC. As shown at 00:00 UTC, the satellite-retrieved polluted-plumes (AOT > 1) from the Siberian wildfire reached the coast of the Hokkaido region and northeastern Japan. As shown by satellite results, NICAM predicted that the same plume would reach the coast of the Hokkaido region. Hereafter, this plume is

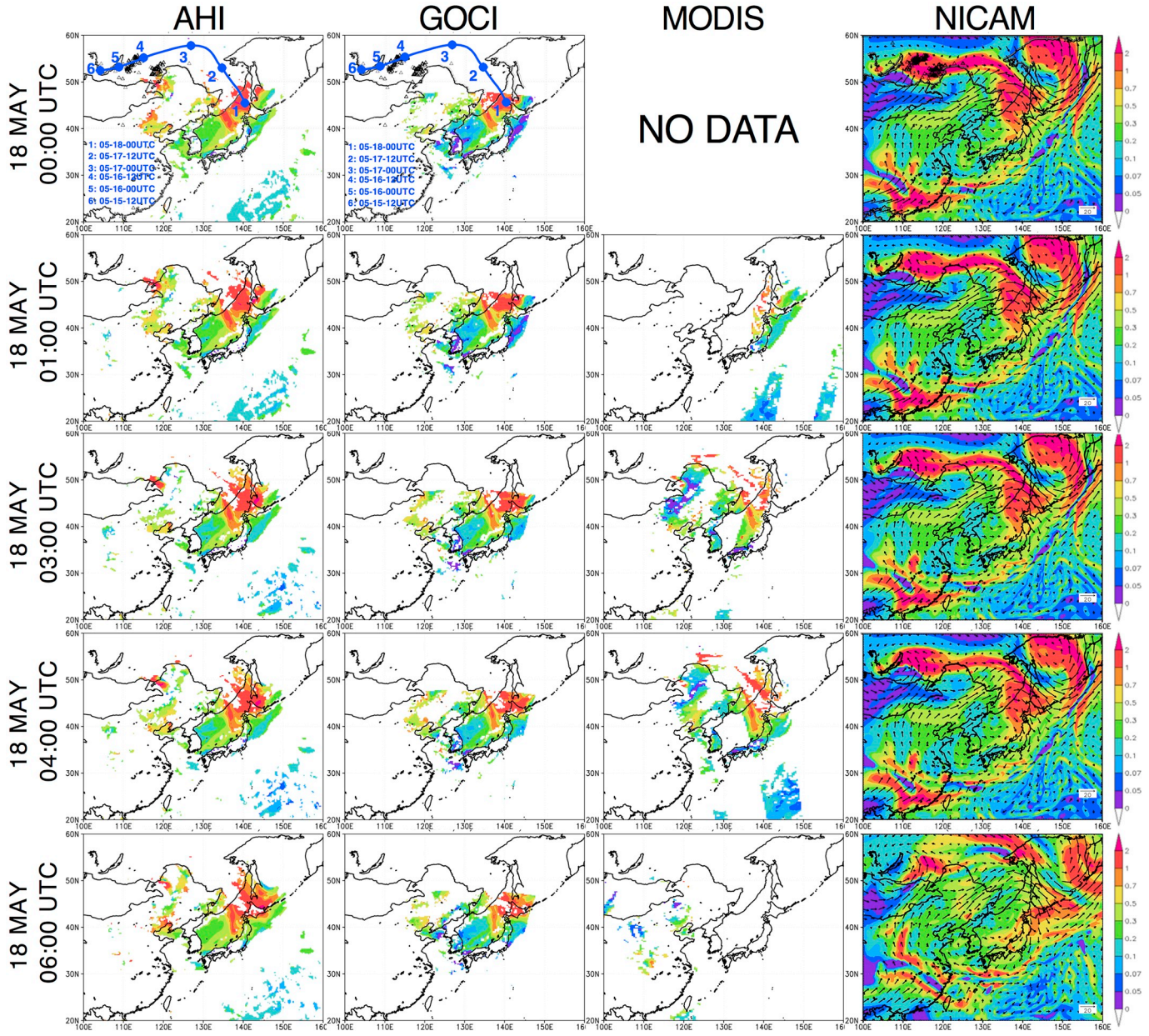

Fig. 2. AHI-retrieved, GOCI-retrieved, MODIS-retrieved and NICAM-simulated AOT values over East Asia. The time was 00:00 UTC or 09:00 JST (Japanese Standard Time), 01:00 UTC or JST 10:00, 03:00 UTC or 12:00 JST, 04:00 UTC or 13:00 JST, and 06:00 UTC or 15:00 JST on 18 May 2016. The MODIS-retrieved AOT values on 00:00 UTC or 09:00 JST are undefined in all areas. The black-triangle marks on 00:00 UTC in AHI and GOCI represent fire spots derived from FIRMS on a daily average of 16 May 2016. On the same panels, the blue line represents the HYSPLIT backward trajectory (Stein et al., 2015; Rolph et al., 2017) started from 00:00 UTC on 18 May at 2 km height over the oceans (145°E, 45°E). The vectors in the panels of NICAM show wind direction and speed at a height of approximately 2 km. (For interpretation of the references to colour in this figure legend, the reader is referred to the web version of this article.)

called 'plume 1.' At the same time, the AHI, GOCI and MODIS data showed that a branch of the polluted plume (AOT > 1) reached from its area of origin (135°E, 42°N) to the Sea of Japan. This plume is called 'plume 2' in this study.

At 06:00 UTC on 18 May, both the AHI- and GOCI-retrieved plume 1 arrived at the eastern edge of Hokkaido, even though MODIS was unable to retrieve it, suggesting that plume 1 was transported across Hokkaido (approximately 200 km) in approximately 6 h. During the same period, such as 04:00 UTC on 18 May, the AHI and GOCI captured high AOT values over land in Hokkaido. At 06:00 UTC on 18 May, plume 1 covered most of the Hokkaido region, and the head of plume 1 reached Iturup Island to the northeast of Hokkaido. The AHI-, GOCI- and MODIS-retrieved AOT values over land in Hokkaido were often undefined because of the high surface albedo over land and cloud contamination. This result implies that polar-orbiting satellites with one or two observations per day would not have observed plume 1 crossing over Hokkaido, demonstrating an important advantage of using next-generation geostationary satellites, which can observe the AOT at a higher temporal resolution than previous satellites; they can also be used for model evaluation over large areas. The transport of the plume 1 captured by these satellites was fairly reproduced by NICAM.

The retrieved plume 2 was horizontally distributed along the northwest-southeast direction at 00:00 UTC on 18 May. At 06:00 UTC, the retrieved plume 2 was distributed in the north-south direction. The retrieved plumes with high AOT values (> 1) did not reach land in northeastern Japan. The time evolution and the peak value of the retrieved plume 2 was successfully simulated by the NICAM. The AHI and GOCI data enabled us to evaluate the model performance while

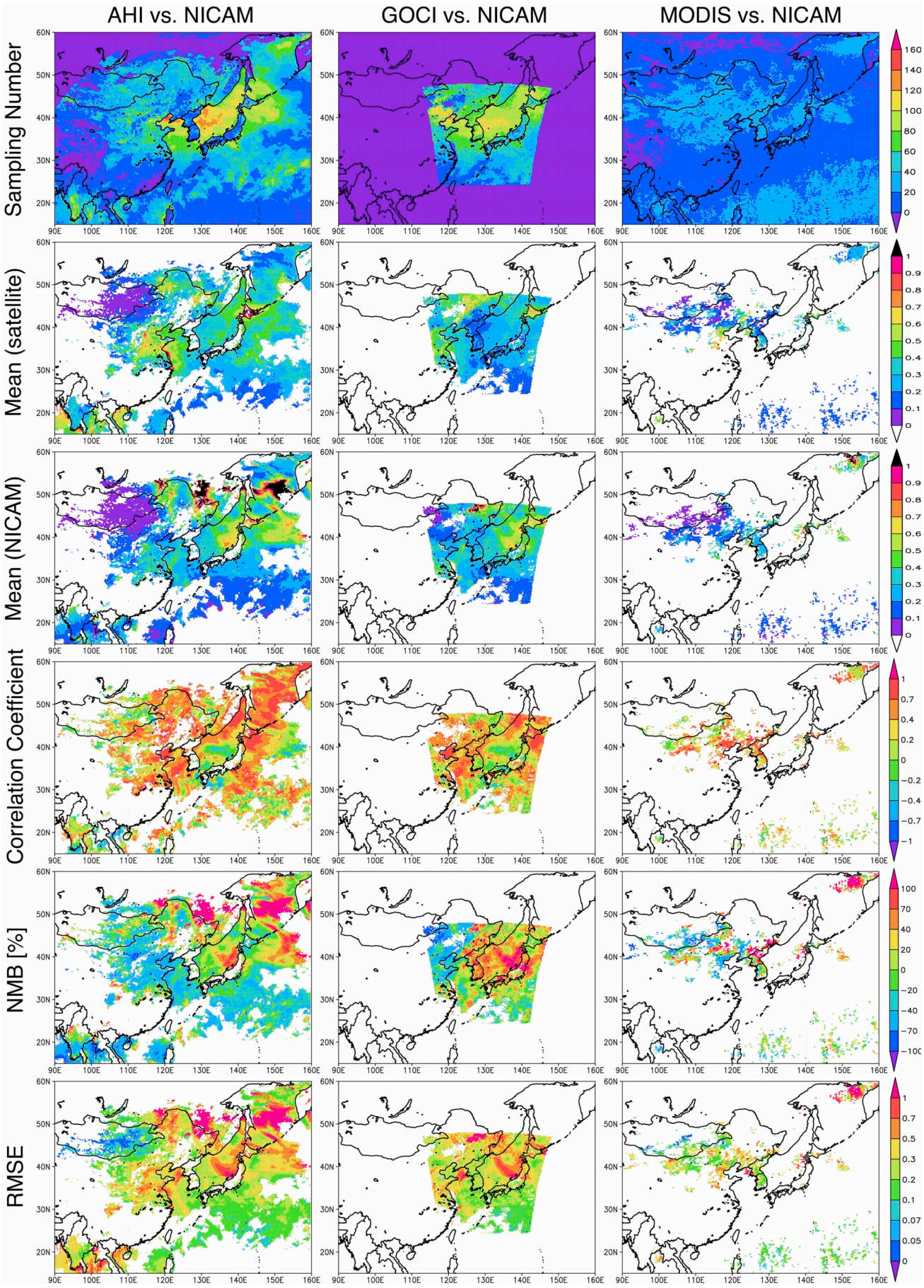

(caption on next page)

Fig. 3. Horizontal distributions of the statistical metrics when using 1-hly datasets between AHI-retrieved and NICAM-simulated AOT values (AHI vs. NICAM), GOCI-retrieved and NICAM-simulated AOT values (GOCI vs. NICAM), and MODIS-retrieved and NICAM-simulated AOT values (MODIS vs. NICAM): sampling numbers from the satellite-retrieved AOT, monthly mean AOT from the satellites, monthly mean AOT simulated by the NICAM, correlation coefficient between the satellite-retrieved AOT and NICAM-simulated AOT with the significant level of 0.05, normalized mean bias (NMB) in percentage between the satellite-retrieved AOT and NICAM-simulated AOT, root-mean-square error (RMSE) between the satellite-retrieved AOT and NICAM-simulated AOT during May 2016. The panels of the mean, correlation coefficient, NMB, and RMSE in the grid where sampling numbers were < 25 are undefined.

focusing on the transport of the plume within approximately 6 h of its initiation, which could be important to precisely forecast air pollution.

Unfortunately, high temporal resolution geostationary satellites cannot retrieve the AOT over areas covered by optically thick clouds associated with low pressure in the midlatitude regions. For example, the AHI-retrieved AOT values were mostly undefined in the Pacific region in Fig. 2. In contrast, NICAM simulated moderately polluted AOT plumes in front of the lows. These plumes cannot be observed from space with the currently available techniques and devices, so model evaluation of cloudy regions should be performed in future studies. To tackle this issue, an aerosol assimilation technique could provide a more reliable distribution of aerosols by using both a model and measurements (Dai et al., 2014; Yumimoto et al., 2016).

4.2. Monthly mean AOT (May 2016)

In this section, we focus on the monthly mean AOT over East Asia. Fig. 3 shows the horizontal distributions of the statistical metrics between satellites and NICAM when using one-hour datasets of AOT values. The top panel in Fig. 3 shows the sampling numbers that were obtained from the AHI-retrieved AOT during May 2016, which indicates that the maximum number of samples in the grid was approximately 150. In AHI, as well as GOCI, the number over the ocean is larger than that over land, since the retrieval of AOT over ocean is relatively easy in the lower surface albedo. In AHI, the presence of clouds caused the number of samples to exceed 8 in 93% of the target area (115°E–155°E, 20°N–50°N) in Fig. 3; the number of samples exceeded 8 in 93% of the area, 20 in 75% of the area, and 40 in 48% of the area, reaching a maximum of 150 and typically ranging from 60 to 120 in the Sea of Japan. The number of AOT samples from the AHI was much greater than that from MODIS onboard the polar-orbiting satellites, which can retrieve AOT only once or twice per day. The second row of panels from the top in Fig. 3 illustrate the horizontal distributions of the monthly mean AOT that were retrieved from the AHI and simulated by the NICAM. The NICAM-simulated AOT was averaged by using grids where and when the AHI could retrieve the AOT. The third, fourth, and fifth rows of panels from the top in Fig. 3 show relevant statistical metrics – the correlation coefficient, NMB, and RMSE – of the AOT between the satellites and NICAM. The definitions of these metrics are explained in Section 2. The results in the grid where the sampling numbers were fewer than 25 are undefined in the panels. The correlation coefficients are shown in the region with the significant level of 0.05.

The monthly mean AOT was 0.36 (AHI) and 0.34 (NICAM). In panels (a) and (b) of Fig. 4, the horizontal distributions of the monthly mean AOT values ranged from 0.2 to 0.4 over the ocean around Japan. However, some local differences existed between the AHI and NICAM. In eastern China around Shanghai, for example, the AHI-retrieved AOT exceeded 0.6, whereas the NICAM-simulated AOT was < 0.5. In contrast, the AHI-retrieved AOT was lower than the NICAM-simulated AOT in regions such as the Sea of Japan and areas north of approximately 50°N. In the Sea of Japan, the AHI-retrieved AOT was < 0.5 without any remarkable high-AOT areas, whereas the NICAM-simulated AOT reached 0.8 with a maximum area around 140°E and 40°N. The overestimation of the NICAM-simulated AOT was probably caused by the overestimation of Siberian biomass burning, which is explained in Section 4.4 using the sensitivity tests with and without biomass burning from the Siberian area. Over land in Hokkaido, the AHI-retrieved AOTs were high with the values of up to 1, the GOCI-retrieved AOT values were 0.6–0.8 and the NICAM-simulated AOT values were 0.6–0.9. The higher AOT values are also deeply analyzed in Section 4.4.

The correlation coefficients between the AHI and NICAM exceeded 0.4 in most of the target area and 0.7 in the northern areas (approximately 45°N) where dense aerosols on 18 May 2016 were transported from Siberian biomass burning. In contrast, the correlation coefficients were negative around the Sea of Japan and Kyushu Island, which suggests that temporal variations in the AHI-retrieved AOT were not adequately captured by the NICAM. In panel (c) in Fig. 4, the values of the correlation coefficient exceeded 0.4 (significant level of 0.05) in 50% of the target area (115°E–155°E, 20°N–50°N) and 0.2 (significant level of 0.05) in 71% of the target area. In panel (d) in Fig. 4, the NMB values were within 20% in 40% of the target area and within 30% in 59% of the target area. In panel (e) in Fig. 4, the RMSE values were < 0.2 in 47% of the target area. In the areas where the NMB and RMSE values were relatively larger, the NICAM-simulated AOTs were larger than the AHI-retrieved values, or the correlation coefficients were negative, such as in the Sea of Japan.

A similar analysis for the monthly mean values of various statistical metrics was performed using NICAM and GOCI (the second column of the panels in Fig. 3). The top panel in Fig. 3 shows the sampling numbers for the GOCI-retrieved AOT during May 2016. The number of samples was generally higher over the land and lower over the oceans than for AHI. The monthly mean AOTs retrieved by the GOCI were generally lower than those retrieved by the AHI. The monthly mean AOT was 0.30 (GOCI) and 0.33 (NICAM, when considering the spatiotemporal collocation with GOCI). Fig. 4 shows that for most ocean areas, including the Sea of Japan, the NICAM-simulated AOT was higher than the GOCI-retrieved AOT (and also higher than the AHI-retrieved AOT). In eastern China near Shanghai, however, the GOCI-retrieved AOT was lower than the AHI-retrieved AOT, and the NICAM-simulated AOT was still lower than the GOCI-retrieved AOT. Over the Korean Peninsula, similar differences in AOT between AHI and GOCI were present. These differences are caused by variations in the observation wavelengths and retrieval algorithms over land. While these differences are important, they are beyond the scope of the present study.

As shown by the comparisons between the AHI and NICAM, the statistical results were generally similar to those between the GOCI and NICAM. The correlation coefficients exceeded 0.4 (significant level of 0.05) for 42% of the target area and 0.2 (significant level of 0.05) for 67% of the target area. The NMB values were within 20% in 46% of the target area and 30% in 61% of the target area. The RMSE values were < 0.2 in 37% of the target area. Comparing the AOT between the GOCI and NICAM also indicates that in the areas where the NMB and RMSE values were larger, such as in the Sea of Japan, the NICAM-simulated AOT was greater than the GOCI-retrieved values, or the correlation coefficients were negative.

Fig. 3 also illustrates MODIS-retrieved AOT and the statistical metrics between MODIS and NICAM. The number exceeded 8 in 93% of the target area, 24 in 39% of the target area, and 40 in 0% of the target area. Due to the limited number of the samples, the statistical metrics were calculated in the following four areas: the coast in Hokkaido (138°E, 42°N), the Korean Peninsula, the Hebei area in China, and Inner Mongolia in China. At the coast in Hokkaido, the NICAM-simulated AOT were overestimated compared to the MODIS-retrieved one. The NMB and RMSE were higher than those in the other areas, as shown in

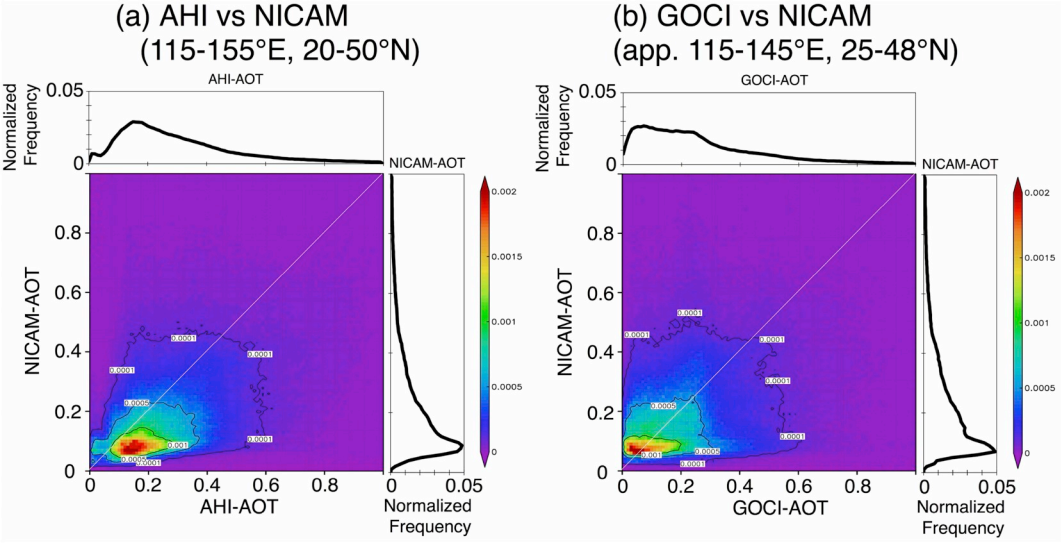

Fig. 4. (a) Scatterplots between the AHI-retrieved and NICAM-simulated AOT and (b) between the GOCI-retrieved and NICAM-simulated AOT when using 1-h datasets. The target region was 115°E–155°E, 20°N–50°N for AHI and 116°E–146°E, 24°N–48°N for GOCI. The probability distribution function (PDF) is shown for the AHI-retrieved, GOCI-retrieved, and NICAM-simulated AOT in May 2016.

the comparison between AHI, GOCI and NICAM. In the Republic of Korea, the NMB and RMSE between MODIS and NICAM were low, whereas those between GOCI and NICAM were relatively high. The differences are not likely caused by the difference in the retrieval technique but rather by the number of samples. In the Hebei area, the correlation coefficients were generally higher, but the NMB was high around Beijing and low near the coast. These were also consistent with the comparison between AHI (and GOCI) and NICAM. In Inner Mongolia, the NICAM-simulated AOT is generally underestimated compared to the MODIS-retrieved one. This finding is also consistent with the comparison between AHI (and GOCI) and NICAM. Therefore, the model evaluation using AHI or GOCI is reliable and more powerful than that using only MODIS, due to the large sample number.

Fig. 4 (a) and (b) respectively show scatterplots of the AHI-retrieved and NICAM-simulated AOT and of the GOCI-retrieved AOT and NICAM-simulated AOT. In the figures, one-hour datasets were used to determine the probability of the AOT in the target area (115°E–155°E, 20°N–50°N), though a limited area was used for GOCI (116°E–146°E, 24°N–48°N) due to its coverage area. In the scatterplot between the AHI-retrieved and NICAM-simulated AOT, the maximum frequency occurs below the one-to-one line, which means that the NICAM-simulated AOTs were underestimated compared to the AHI-retrieved values. The maximum in the PDF ranged from 0.05 to 0.1 in the NICAM-simulated AOT, whereas the maximum ranged from 0.10 to 0.20 in the AHI-retrieved AOT. The monthly means of the AHI-retrieved and NICAM-simulated AOT were 0.36 and 0.34, respectively. The correlation coefficient was calculated to be 0.39 (significant level of 0.05). In contrast, the maximum frequency between the GOCI-retrieved and NICAM-simulated AOTs occurred on the one-to-one line, but the maximum in the PDF ranged from 0.03 to 0.1 in the GOCI-retrieved AOT. The monthly means of the GOCI-retrieved and NICAM-simulated AOT were 0.30 and 0.33, respectively, when estimated using the grids and times where the GOCI-retrieved AOT was obtained over the limited area (116°E–146°E, 24°N–48°N). The correlation coefficient was 0.26 (significant level of 0.05).

The PDF in the AHI-retrieved AOT produced +2.07 skewness and 9.16 kurtosis, whereas the PDF in the NICAM-simulated AOT produced +6.00 skewness and 91.24 kurtosis. The skewness in NICAM was 3 times larger than that in the AHI. The kurtosis in NICAM was 10 times larger than that in the AHI. These differences in the skewness and kurtosis for the normalized frequency of AOT between the AHI and NICAM are similar to those obtained from the GOCI and NICAM. The two NICAM values exhibit a narrower PDF distribution compared to those from both the AHI and GOCI (Fig. 4). In Fig. 4, when the normalized frequency exceeds 0.001, the NICAM-simulated AOT ranges from 0.05 to 0.10, the AHI-retrieved AOT ranges from 0.10 to 0.25, and the GOCI-retrieved AOT ranges from 0.00 to 0.20. These results suggest that the AHI-retrieved and GOCI-retrieved AOTs were spatiotemporally scattered compared to the NICAM-simulated AOT. As mentioned before, the differences in the AOT between the AHI and NICAM or between the GOCI and NICAM can be attributed to differences in the transboundary aerosols from both biomass burning and anthropogenic effects. In other words, the NICAM-simulated aerosols were overestimated over the ocean, especially the Sea of Japan, and underestimated in eastern China and the outflow areas. Therefore, these opposite signals canceled the difference between the monthly mean values in NICAM and the geostationary satellites over the target region.

To analyze the regional dependence of the PDF, we introduced the PDF and quantified parameters in various sub-regions, which were regularly selected every 10° within the rectangular area of 115°E–155°E and 20°N–50°N. For the 12 sub-regions of the target region, Fig. 5 shows histograms of the 1-hour AOT simulated by the NICAM and retrieved from each geostationary satellite. Fig. 5 includes information regarding the statistical metrics for the NICAM, AHI, and GOCI. There are two lines for NICAM, because there may be some differences between the monthly mean values due to variations in spatiotemporal sampling, i.e., from AHI or GOCI defined datasets (Schutgens et al., 2016). All the panels in Fig. 5 show that the differences between two NICAM results are generally small, so the gaps caused by different spatiotemporal sampling are small. As mentioned in the previous paragraph, the NICAM-simulated aerosols were overestimated over the ocean, especially the Sea of Japan, likely due to the overestimation of aerosols from Siberian biomass burning. The aerosols transported the northern region (125°E–155°E and 40°N–50°N; the A12, A13, and A14 areas in Fig. 5) on 18 May 2016, and the May mean values of the NICAM-simulated AOT in A12, A13, and A14 tended to be higher compared to the satellite-retrieved ones. In both A13 and A14, the PDF for the NICAM-simulated AOT fell within the range of the PDFs for the AHI- and GOCI-retrieved AOT. For A12, the AHI-retrieved AOT was much higher than the GOCI-retrieved AOT, probably due to differences between the observation wavelengths and retrieval algorithms over land. Overall, the expected features of the AOT distributions, which gradually decreased from land

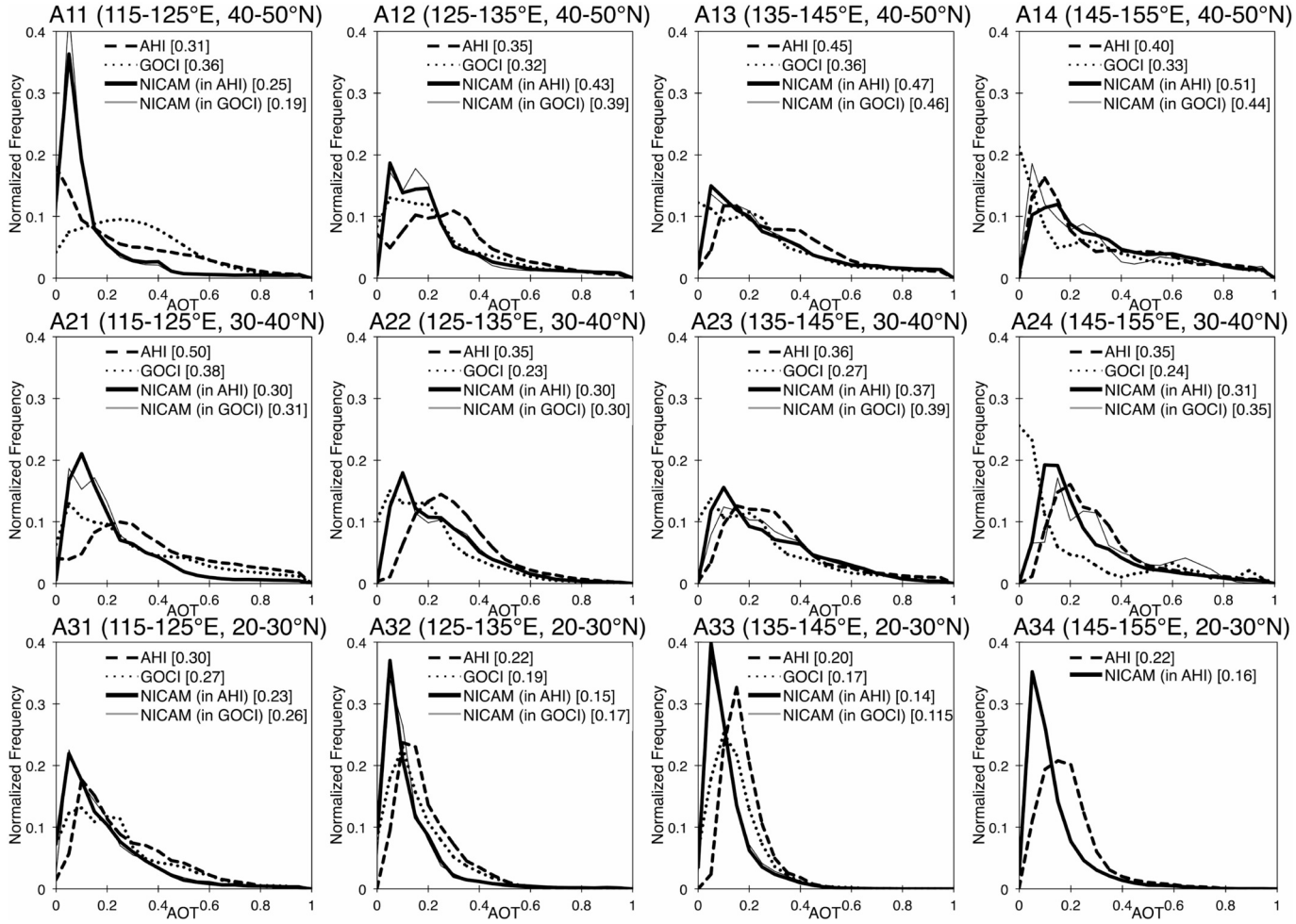

Fig. 5. Probability distribution functions (PDFs) for the AHI-retrieved, GOCI-retrieved, and the two NICAM-simulated AOTs in May 2016 for the 12 sub-regions within the target region (115°E–155°E, 20°N–50°N). "NICAM (in AHI)" indicates that NICAM used the spatiotemporal collocation with AHI datasets; "NICAM (in GOCI)" indicates that NICAM used the spatiotemporal collocation with GOCI datasets. The numbers in the bracket represent regional averages of AOT in each area.

(A12) to ocean (A13 and A14), are not clear in the AHI, GOCI and NICAM.

Since the NICAM-simulated aerosols were underestimated in eastern China and the outflow areas as shown in Fig. 3, the AOT in the A21 areas in Fig. 5 was focused. At A21, the highest AOTs in the AHI were found over land. The monthly mean value of the AHI-retrieved AOT was 0.50, which was approximately 0.20 larger than that of the NICAM-simulated AOT. The correlation coefficient was a moderate value of 0.42, and the temporal variations in the AHI-retrieved and NICAM-simulated AOTs generally coincided. The monthly mean value of GOCI-retrieved AOT at A21 was 0.38, which is larger than that simulated by NICAM. The correlation coefficient was a moderate value of 0.37. Although this result of the highest AOT values in the AHI may be partially caused by retrieval bias over land (Yoshida et al., 2018), higher AOTs at A21 can be expected in the East Asia Sea, so the AHI-retrieved AOT is within the uncertainty of the retrieval. Therefore, the difference in the AOT between the AHI and NICAM may have been caused by a missing aerosol component such as nitrate or anthropogenic secondary OC, which have been increasing in recent years in China (e.g., Park et al., 2011; Hu et al., 2017).

Around Japan, except for the northern parts of Japan in both A22 and A23, regional differences in the PDF were small and were similar to those throughout the target area, as shown in Fig. 4. However, the NICAM-simulated AOT at the maximum value of the PDF for A22 and A23 was lower than that from the AHI. The skewness of NICAM was over twice that of the AHI. The kurtosis of NICAM was over 5 times larger than that of the AHI. The GOCI-derived PDFs at A22 and A23 had lower skewness and kurtosis compared to the NICAM-derived PDFs. The results for the whole of Japan including A13, A21 and A22 areas suggested that the differences between the AHI-retrieved, GOCI-retrieved and NICAM-simulated AOT occurred not in specific regions but rather over broader areas.

In the southern region (115°E–155°E and 20°N–30°N; the A31, A32, A33, and A34 areas in Fig. 5), the AOTs were lower than those in the other areas, in part because of the lower aerosol loadings and in part because of the lower sampling number under cloudy conditions. At A31, which is the closest to land within the southern region, the monthly mean value of the AHI-retrieved AOT was 0.30, whereas that of the NICAM-simulated AOT was 0.23. These values were higher than those over the ocean (at A32, A33, and A34) in the southern region. Over the ocean, the NICAM-simulated AOT was up to 0.06 lower than the AHI-retrieved AOT. However, the skewness and kurtosis from NICAM were still higher than those from the AHI. This feature was similar in the comparisons in the northern and middle regions. In the southern region, the AOT mean values of the GOCI-retrieved AOT were slightly higher than those of the NICAM-simulated AOT by 0.01–0.02, although the sampling numbers are limited. Comparing the PDFs of the AHI, GOCI, and NICAM shows that the NICAM-derived PDF was lower than the AHI- and GOCI-derived PDFs in the southern region. Therefore, some bias from outflow aerosols from the continent or background aerosols in NICAM may influence the total AOT in May 2016.

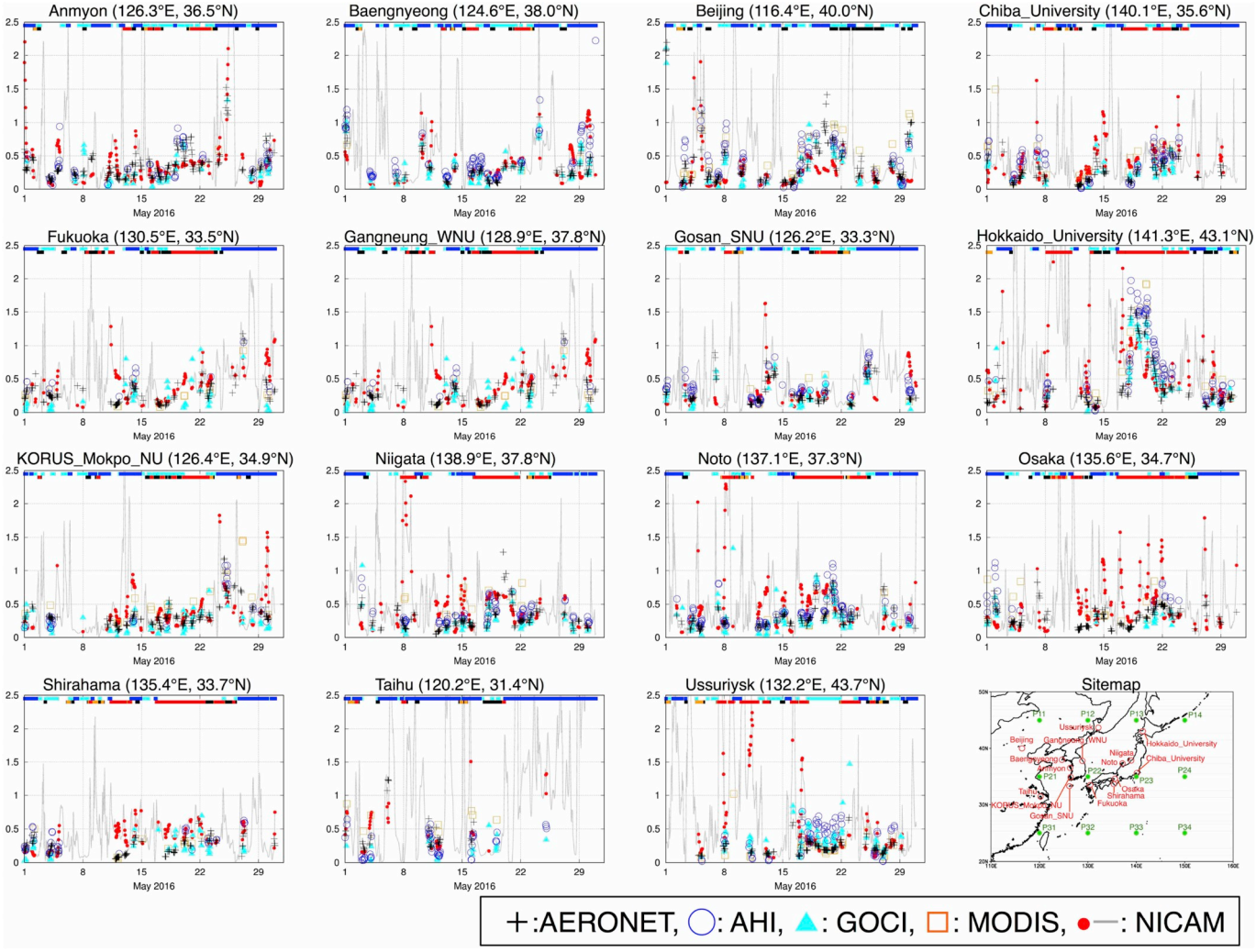

Fig. 6. Hourly variations in the AOT as retrieved from the ground-based measurement (AERONET with plus symbols in black), geostationary satellites (AHI with circle symbols in blue and GOCI with triangle symbols in cyan), the polar-orbiting satellites Terra and Aqua (MODIS with square symbols in orange), and simulated by NICAM (closed circle in red symbols indicates results for which AERONET, AHI, GOCI, or MODIS detected AOT and the gray line represents all NICAM results) in May 2016 at the selected AERONET site in East Asia. The marks of closed squares in masses around the top in each panel represent the periods of the high contribution of sulfate in blue (> 30% of the total AOT) and in cyan (> 50% of the total AOT) to the total AOT and those in the high (> 50%) contribution of carbonaceous aerosols in black (for all carbon), in orange (for non-Siberian biomass burning), and in red (for Siberian biomass burning) to the total AOT, respectively. The bottom-right panel shows a sitemap for the selected AERONET sites in red and the selected points in green used in this comparison. (For interpretation of the references to colour in this figure legend, the reader is referred to the web version of this article.)

4.3. Temporal variations in the AOT

The advantages of using geostationary satellites include not only estimating the spatial averages of AOT using a larger number of samples but also comparing the temporal variations in AOT at any place with model results. In this section, we compare the temporal AOT as retrieved by AERONET, AHI, GOCI and MODIS and as simulated by NICAM at the selected AERONET sites (Fig. 6). The comparisons were also conducted at the 12 selected points (P11, P12, P13, P14, P21, P22, P23, P24, P31, P32, P33 and P34) in the regularly selected area used in Fig. 5 where no AERONET sites are located, but the places can be used as a model evaluation using the geostationary satellites (Fig. 7).

The heavy air pollution from Siberian wildfires was transported to northern Japan on 18 May 2016. As shown in Fig. 2, the satellite-retrieved AOT was successfully reproduced by NICAM. In some areas, such as the Sea of Japan, however, the horizontal distributions of the satellite-retrieved AOT in the monthly average were different from those simulated by NICAM (Fig. 3). We first attempt to understand the difference in AOT between satellites and NICAM at the relevant AERONET sites, i.e., Hokkaido_University, Niigata and Noto, and the relevant points over the ocean (P13 and P14). On 18 to 22 May at Hokkaido_University, the timings of the strong peak as retrieved by the satellites were close to those obtained by AERONET. On 18 May, the maximum value of the GOCI-retrieved AOT was approximately 1.5, which was comparable to or somewhat lower than that obtained by AERONET. That of the AHI-retrieved AOT reached 2 on 18 May and tended to be overestimated compared to AERONET results on the polluted days (18 to 22 May). The MODIS-retrieved AOT was limited but comparable to the AERONET results, except for one result on 20 May. From 18 to 22 May, the AOT values decreased to 0.25. At P13 over ocean near Hokkaido_University, a strong AOT peak was retrieved by both AHI and GOCI. At P14 over the ocean located at the east of Hokkaido, a strong peak with AOT values of > 1.5 was retrieved by AHI (GOCI cannot cover P14). At Niigata and Noto, located at the coast of the Sea of Japan, the associated high-AOT peaks were retrieved by the AERONET and satellites on 19–21 May. During these days at the relevant sites, NICAM-simulated AOT from Siberian biomass burning was a major component, as shown by the colored bars in each panel in

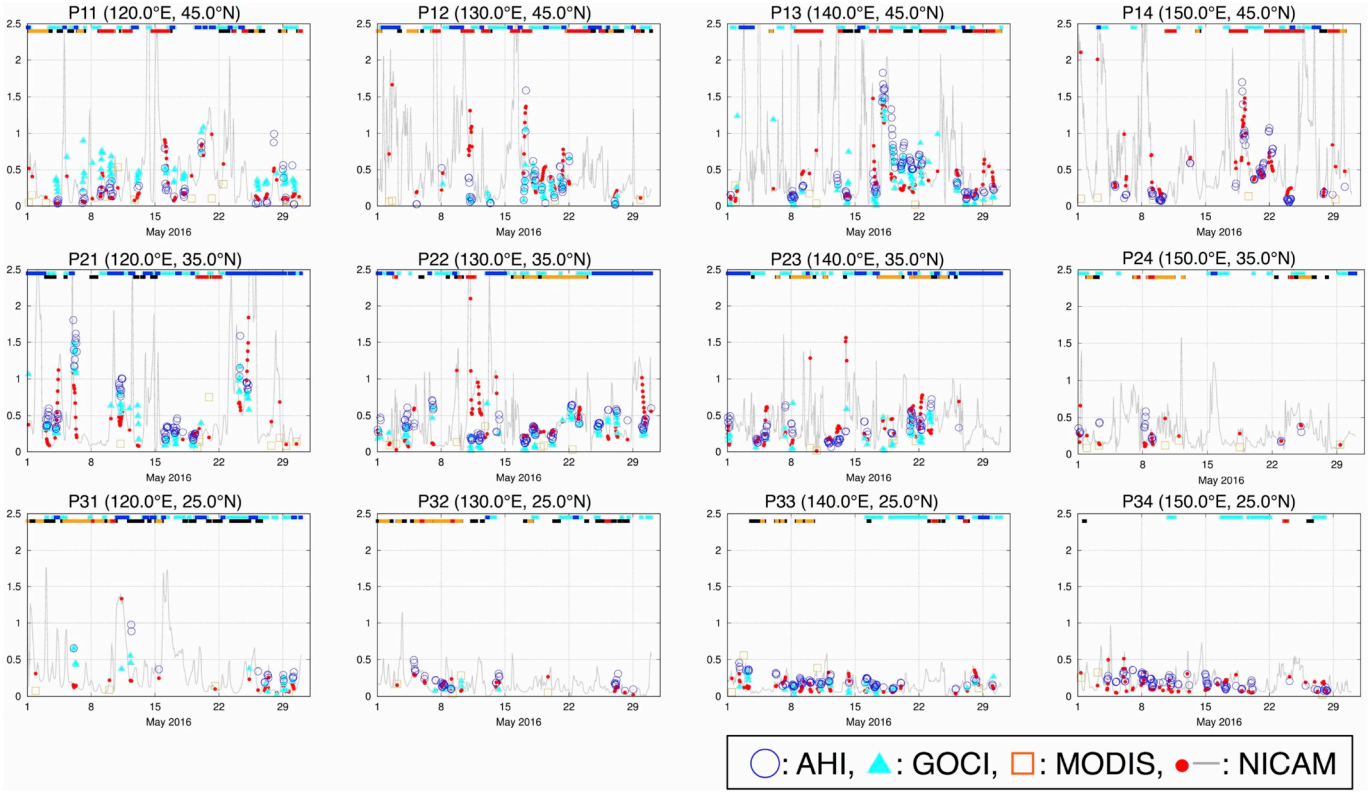

Fig. 7. The same as in Fig. 6, but for the different site where AERONET cannot be established. The locations of the comparison site are shown in the bottom-right panel of Fig. 6. These sites are centers of the focusing area in Fig. 5, e.g., P11 (120.0°E, 45.0°N) is the center point of A11 (115°E–125°E, 40°N–50°N) in Fig. 5.

Figs. 6 and 7. Overall, the heavy air pollution from Siberia to Japan was clearly captured by the AERONET and satellites and was generally reproduced by NICAM, but with two differences. One is that the strong peak in the simulated AOT occurred earlier at Hokkaido than that captured by AERONET and the satellites. The other is that the magnitudes of the simulated AOT during 18–22 May near Hokkaido tended to be slightly underestimated compared to those obtained by both AERONET and the satellites.

On the other days in May 2016, especially 8 May 2016, only NICAM simulated sharp peaks with excessively high AOT values (> 2) associated with Siberian biomass burning at the relevant sites, whereas both AERONET and the satellites retrieved these peaks with high AOT values (< 1). Except for these days, NICAM generally reproduced the AERONET- and satellite-retrieved AOTs. During the whole month, the NMB values between AERONET and NICAM were estimated to be +22% (Hokkaido_University), +100% (Niigata) and +55% (Noto), as shown in Table 1. In Table 1, the RMSE values were also calculated to be 0.45 (Hokkaido_University), 0.94 (Niigata) and 0.47 (Noto). At P13, the NMB and RMSE values of AOT between the two geostationary satellites and NICAM were calculated to be −3% to +11% and 0.49 to 0.61, respectively (Table 1). These overestimations by NICAM were probably caused by the larger peak values of the simulated AOT from Siberian biomass burning on the specific days during May 2016.

The air pollutants from Siberia to Japan were also likely transported over the following sites: Ussuriysk and P12. On 17 May, a strong peak in the AERONET-retrieved AOT with a value of 0.7 was found at Ussuriysk. The high AOT values decreased to 0.2 on 20 May. The temporal variations in the AERONET-retrieved AOT were comparable to those obtained by AHI, GOCI and MODIS, but the magnitudes of the retrieved AOT were slightly different among the retrieved results. The AHI-retrieved and GOCI-retrieved AOTs tended to be higher than the AERONET-retrieved one. Using the monthly mean value as shown in Fig. 3, the NMB value between AHI or GOCI and AERONET was calculated to be +42% (AHI) and + 33% (GOCI), respectively (Table 1). The MODIS-retrieved AOT was comparable to the AERONET result. The NICAM-simulated AOT was also comparable to the AERONET one, especially during 18–22 May, but the peak values of the NICAM-simulated AOT on 8, 10 and 17 May were overestimated. The major component of the NICAM-simulated AOT was the aerosol from Siberian biomass burning. This tendency is also consistent to that obtained at P12. As a result, at Ussuriysk the NMB value between AERONET and NICAM was calculated to be +92%, whereas at P12 the NMB value between the two geostationary satellites and NICAM was calculated to be +70% to +76% (Table 1). This exception of the overestimation of the simulated AOT mainly from Siberian biomass burning at Ussuriysk and P12 on 16–17 May also caused the overestimation of the simulated AOT at Hokkaido_University on 17–18 May.

In western Japan, the transboundary air pollutants of anthropogenic sources from the continents are expected to arrive in spring [Goto et al., 2015b]. We focus on the four relevant sites in western Japan: Fukuoka, P22, Osaka, and Shirahama. In Fig. 3 of the monthly mean values, the correlation coefficients between GOCI and NICAM were calculated to be 0.2–0.4 at the northern part of Kyusyu Island (in these areas, the AHI did not provide the correlation coefficient with NICAM due to the limited sampling number). Over oceans around this area, the correlation coefficients between AHI or GOCI and NICAM were < 0.2 on a monthly average. At Fukuoka, the spikes in NICAM-simulated AOTs were generally comparable to the those obtained by AERONET, except for the overestimation on 10 and 30 May. The model results showed that most of the strong peaks were caused by carbonaceous aerosols from Siberian biomass burning on 10 May and anthropogenic sulfate on 30 May. On the monthly average, the NMB and RMSE values using AERONET and NICAM results were calculated to be +27% and 0.29, respectively. At P22 over oceans near Fukuoka, the NMB and RMSE values using the two geostationary satellites and NICAM results were calculated to be +15% to +78% and 0.37 to 0.54, respectively

Table 1
Statistical metrics (sampling number or N, correlation coefficient or R, normalized mean bias or NMB, and root-mean-square-error or RMSE) between NICAM and AHI/GOCI/AERONET at the selected AERONET sites and the selected points in May 2016.

Variables	N			R			NMB [%]			RMSE			Location	
Retrieved	AHI	GOCI	AERONET	AHI	GOCI	AERONET	AHI	GOCI	AERONET	AHI	GOCI	AERONET	LON	LAT
Anmyon	57	48	231	0.45	0.66	0.55	−23	−2	−3	0.22	0.20	0.28	126.330	36.539
Baengnyeong	101	76	138	0.36	0.45	0.45	−25	44	33	0.46	0.47	0.38	124.630	37.966
Beijing	91	58	212	0.54	0.22	0.32	−47	−42	−47	0.33	0.41	0.43	116.381	39.977
Chiba_University	72	41	149	0.27	0.15	0.29	−2	53	51	0.27	0.28	0.30	140.104	35.625
Fukuoka	14	55	128	0.38	−0.03	0.29	−27	59	27	0.26	0.34	0.29	130.475	33.524
Gangneung_WNU	118	98	226	0.54	0.45	0.17	1	60	31	0.24	0.29	0.32	128.867	37.771
Gosan_SNU	83	46	129	0.51	0.53	0.40	−13	10	9	0.21	0.19	0.26	126.162	33.292
Hokkaido_University	93	51	178	0.73	0.73	0.45	−31	−10	22	0.45	0.31	0.45	141.341	43.075
KORUS_Mokpo_NU	30	71	173	0.35	−0.03	0.27	−1	77	18	0.34	0.39	0.32	126.437	34.913
Niigata	75	57	173	−0.20	−0.19	−0.10	108	188	100	1.21	1.22	0.94	138.942	37.846
Noto	107	85	163	−0.12	−0.14	0.01	36	73	55	0.48	0.57	0.47	137.137	37.334
Osaka	22	26	18 × 2	0.25	−0.15	0.24	−42	35	46	0.42	0.27	0.36	135.591	34.651
Shirahama	37	44	109	0.42	0.45	0.03	−12	45	50	0.17	0.19	0.24	135.357	33.693
Taihu	52	19	42	0.35	−0.10	0.50	53	90	−7	0.33	0.35	0.27	120.215	31.421
Ussuriysk	64	76	150	−0.11	0.28	0.32	30	60	92	0.60	0.71	0.55	132.163	43.700
P11	58	75	0	0.64	0.57	–	−4	−54	–	0.21	0.30	–	120.000	45.000
P12	46	54	0	0.33	0.48	–	70	76	–	0.44	0.35	–	130.000	45.000
P13	112	89	0	0.34	0.36	–	−3	11	–	0.61	0.49	–	140.000	45.000
P14	80	0	0	0.62	–	–	1	–	–	0.42	–	–	150.000	45.000
P21	83	75	0	0.50	0.54	–	−33	−12	–	0.47	0.38	–	120.000	35.000
P22	108	84	0	−0.28	−0.16	–	15	78	–	0.37	0.54	–	130.000	35.000
P23	80	42	0	0.18	0.15	–	19	47	–	0.29	0.29	–	140.000	35.000
P24	19	0	0	−0.17	–	–	−33	–	–	0.22	–	–	150.000	35.000
P31	17	17	0	0.42	0.18	–	−61	−30	–	0.31	0.33	–	120.000	25.000
P32	35	6	0	0.72	−0.44	–	−25	4	–	0.09	0.08	–	130.000	25.000
P33	83	36	0	0.41	0.09	–	−38	−16	–	0.11	0.11	–	140.000	25.000
P34	90	0	0	0.32	–	–	−27	–	–	0.11	–	–	150.000	25.000

(Table 1). There, values were smaller than those obtained at the upper area of the outflow, such as Gosan_SNU, with NMB and RMSE values of +9% and 0.26, respectively (Table 1). At Osaka, located approximately 600 km east of Fukuoka, the NICAM-simulated AOT provided sharp peaks during 11–22 May and was overestimated compared to the AERONET results, with an NMB value of +46% and an RMSE value of 0.36 (Table 1). The overestimation was also mainly caused by Siberian biomass burning. At Shirahama, located approximately 100 km south of Osaka, NICAM had the same trend as Osaka and could not adequately reproduce the observation (NMB = +50% and RMSE = 0.24). The overestimation of the NICAM-simulated AOT from Siberian biomass burning at Osaka could cause the overestimation at Shirahama. Therefore, the difficulty in properly simulating the Siberian biomass burning can worsen the reproducibility of the east parts of western Japan.

In the East China Sea, which is closer to the source region of the anthropogenic matters than is Japan, the relevant sites are the following four: Gosan_SNU, Mokpo_NU, Anmyon, and Baengnyeoung. At Gosan_SNU, located approximately 300 km west of Fukuoka, the NICAM-simulated AOT was generally comparable to the AERONET-retrieved and the satellite-retrieved AOT, but there were two unrealistic peak values in the NICAM-simulated AOT on 13 and 30 May. On these days, the overestimation of the NICAM-simulated AOT was caused by anthropogenic sulfate. On 30 May, this overestimation of the simulated sulfate caused the overestimation of the simulated AOT over a large area, at least at the following sites: KORUS_Mokpo_NU, Fukuoka and Gangeung_WNU on the Korean Peninsula adjacent to the Sea of Japan. In Table 1, the correlation coefficient of AOT between AERONET and NICAM was calculated to be +0.40. At the other sites in the East China Sea, the values of the correlation were calculated to be +0.27 (KORUS_Mokpo_NU), +0.55 (Anmyon), and +0.45 (Baengyeong). The NMB values were relatively low with the values of +18% (KORUS_Mokpo_NU), −3% (Anmyon), and +33% (Baengyeong). In the East China Sea, as shown in Fig. 3, the correlation coefficients tended to be higher compared to the other areas, which suggest that NICAM generally succeeded in simulating temporal variations of the anthropogenic aerosols from the continent.

One of the major source areas of anthropogenic matters in East Asia is China, where the relevant sites are Beijing, Taihu, P11 and P21. At the Beijing and Taihu sites, the correlation between the AERONET and NICAM was relatively higher, with the values of 0.32 (Beijing) and 0.50 (Taihu). At the points of P11 and P21, the correlations between the two geostationary satellites and NICAM were also relatively higher, with the values of 0.57 to 0.64 (P11) and 0.50 to 0.54 (P21). Because the Taihu site is located at the top of a mountain, the reason for the difference in the AOT between AERONET and NICAM may be caused by the problem of the representativeness in the comparison grid (0.2° by 0.2°). However, at the other sites (Beijing, P11, and P21), the results reflected the capability of the model to capture the aerosols near the source areas. At these sites, the NICAM-simulated AOT tended to be underestimated compared to the AERONET or the satellite results. The NMB value between AERONET and NICAM was estimated to be −47% (Beijing), whereas the values between the two geostationary satellites and NICAM were estimated to be −54% to −4% (P11) and −33% to −12% (P21). As pointed out in Section 4.2, the underestimation of the NICAM-simulated AOT may be caused by a missing aerosol component, such as nitrate and anthropogenic secondary OC, in China. At the P31 site located at the east coast in China, the sampling number was limited because of cloud contamination in the AHI retrievals, so it is difficult to discuss the results; however, as shown in the Beijing, P11, and P12 sites, the NICAM-simulated AOT tended to be underestimated with the NMB value of −61% to −30%.

At the relevant sites over China, the East China Sea, and western Japan, there was a slight time difference between the retrieved results and NICAM; the simulated AOTs were comparable to the retrieved results but preceded them by several hours. Such differences in timing between NICAM and the retrieved data occurred several times and generally occurred in situations where the meteorological fields, including low and high patterns, were slightly different from those obtained from the real atmosphere. Therefore, comparisons using datasets

with high temporal resolution can suffer because of slight changes in the meteorological fields, especially in the outflow regions such as the East Asia Sea and Japan.

In eastern Japan, the transboundary air pollutants of anthropogenic sources from the continents are sometimes transported but not often [e.g., Goto et al., 2015b]. We focus on the two relevant sites in eastern Japan: Chiba_University and P23. On 21–23 May, the NICAM-simulated AOT were comparable to the AERONET- and the satellite-retrieved AOTs. The NICAM simulated high AOT values from biomass burning during these days. During May 2016, the model tended to be overestimated compared to the AERONET, with an NMB value of +51% (Table 1). At the P23 site, located approximately 70 km south of the Chiba_University site, the NICAM-simulated AOT was overestimated compared to the satellites, but Siberian biomass burning has a small contribution to the total AOT. The NMB value between the two geostationary satellites and NICAM was calculated to be +19% to +47% (Table 1). Therefore, the impacts of the non-Siberian biomass burning in the model were possibly overestimated, but we can say that the impacts of the biomass burning, including Siberian wildfires, in eastern Japan were not as great as those at the Chiba_University site in May 2016. In Section 4.4, we discuss how well NICAM reproduced the real atmosphere in more detail using the surface measurements of PM2.5 as well as the vertical measurements by LIDAR.

Finally, the NICAM-simulated AOTs were evaluated at the outflow areas and remote ocean, i.e., P32, P33 and P34. As already mentioned in Fig. 5, the simulated and retrieved AOTs over the remote ocean areas of A32, A33, and A34 were lower than those at the other sites. These oceanic sites can be considered to show the background aerosol levels. At the center of P32, the AHI-retrieved and NICAM-simulated AOTs decreased at a similar rate and magnitude from 5 to 10 May. In contrast, the P33 and P34 sites, which are typical remote ocean sites, the background AOT levels from NICAM were lower than those from both the AHI and GOCI, although the retrieval accuracy for the background levels was lower than that for highly polluted air masses (e.g., Toth et al., 2013).

4.4. 4-dimensional structure of the aerosols over Japan in May 2016

The unique geostationary satellite datasets enable us to estimate the PDF of the AOT over Japan and compare the results with modeled results. The 1st moment (i.e., the mean) of the PDF from the NICAM-simulated AOTs was generally comparable to that of the geostationary satellites. The correlation coefficient between the geostationary satellite-retrieved AOTs and the NICAM-simulated AOT was moderate to low, and the 3rd and 4th moments of the satellite-retrieved AOTs (i.e., the skewness and kurtosis) differed from those of the NICAM-simulated AOT. This difference was mainly caused by the overestimation of biomass burning from Siberia during May 2016 and the underestimation of anthropogenic (and to some extent background) aerosols, as explained in Section 4. Slight differences in the meteorological fields (such as the positions of areas of low and high pressure) can also be expected to affect the accuracy of the transboundary aerosol distribution. In fact, the slight difference in timing between the aerosol peaks resulted in low correlation coefficients, given the limited number of samples. As follows, we first investigate the 4-dimensional structure of the atmospheric aerosol distributions according to the multiple measured datasets: the two geostationary satellite datasets, in situ PM2.5 measurements, and LIDAR data. Second, we discuss how much NICAM reproduces the 4-dimensional structure of the aerosol obtained by the multiple measurements, especially by focusing on the relationship of aerosols among the following: the column amount, the surface concentration, and the vertical profile during the specific events. The target areas include northern Japan (including Hokkaido and Niigata, as shown in Fig. 8), western Japan (around Fukuoka, as shown in Fig. 9), and eastern Japan (Kantou, including Tokyo, as shown in Fig. 10).

First, we focus on northern Japan, including Hokkaido and Niigata. The left panels in Fig. 8 show the column AOT data from the two geostationary satellites, surface PM2.5 concentrations from in situ measurements, and vertical profiles of the extinction coefficient for the spherical particles from LIDAR. We defined two types of events in terms of the relationship between the AOT and surface PM2.5: (1) the satellite-retrieved AOT was high but the surface PM2.5 concentration was low (event 1) and (2) both the satellite-retrieved AOT and the surface PM2.5 concentration were high (event 2). During May 2016, northern Japan experienced two event 1 cases and one event 2 case. From 7 to 10 May, which included the event 2 case, the observed PM2.5 concentrations exceeded 45 $\mu g\,m^{-3}$, which were the maximum values in northern Japan during May 2016. The GOCI-retrieved AOT was also high, with a value up to 1; the AHI-retrieved AOT was lower, with a value up to 0.5. The LIDAR-retrieved extinction coefficient was at most 0.05 km^{-1}. In contrast, the NICAM-simulated PM2.5 concentrations exceeded 100 $\mu g\,m^{-3}$. The simulated AOT was high, with values above 1.5, and the simulated extinction coefficient reached 2 km^{-1}, each of which was the maximum value during May 2016. From the surface to 3 km in height, the simulated aerosols were overestimated compared to the multiple measurements. The gap between the measurements and NICAM was caused by the overestimation of NICAM-simulated aerosols from Siberian biomass burning, as pointed out in the analysis at the AERONET Hokkaido_University site.

The period of 17–21 May included an event 1 case. The Siberian biomass burning reached Japan on 18 May 2016 (Fig. 2) and was dominant in this event 1 case. The satellite-observed AOT values exceeded 1.5 around Hokkaido. The LIDAR measurements captured a strong peak with a maximum extinction coefficient of 0.5 km^{-1} at a height of 0.5–3.5 km in Niigata. On the same days, the observed PM2.5 concentrations at the surface near Hokkaido were not as high and showed no remarkable spikes, which means that the aerosols from the Siberian biomass burning did not reach the surface. NICAM successfully captured this peak in the satellite-retrieved AOT, but the simulated extinction coefficient was vertically broader than that for the observed value. Apart from the LIDAR results, the bottom of the simulated peak nearly reached ground level (0.5 km). Thus, the NICAM-simulated PM2.5 concentrations at the surface were approximately 20 $\mu g\,m^{-3}$ higher than both those on the other days. The distance between Hokkaido and Niigata is 300 km, so the AOT and vertical extinction coefficients were not exactly consistent. The NICAM-simulated AOT was lower than the satellite-retrieved AOT at Hokkaido, whereas the NICAM-simulated extinction coefficient was higher than the LIDAR-retrieved value at Niigata. This inconsistency was mainly caused by the overestimated simulated AOT at Niigata, as shown in Figs. 3 and 6. In summary, the model captured the transport of aerosols derived from Siberian biomass burning and exhibited AOT values comparable to the observed values, but the vertical profile of the simulated biomass burning aerosols was different from the observed profile, especially near the surface.

During 2–5 May, which was another event 1 case, the satellite-retrieved AOT exceeded 0.8, which was a relatively high value during May 2016. At the surface, however, the observed PM2.5 concentrations were relatively low, with a value of at least 20 $\mu g\,m^{-3}$. The LIDAR-retrieved extinction coefficient was at most 0.2 km^{-1}, even though most of the data was undefined. In contrast, the NICAM-simulated AOT exceeded 0.8, which was also the second-highest value during May 2016. The simulated PM2.5 concentrations reached only 20 $\mu g\,m^{-3}$, which were comparable to the observed values. The simulated extinction coefficient reached 1 km^{-1}, which tended to be higher than that from the LIDAR data. Therefore, NICAM generally captured the 3-dimensional structure of the air pollution, which showed the column burden was higher but the surface loading was lower, from the both AOT and surface measurements, even though the simulated AOTs were overestimated compared to the retrieved AOTs. During this event, the majority of the aerosols were not from biomass burning but sulfate (likely anthropogenic sources). Sulfate was dominant in this event 1

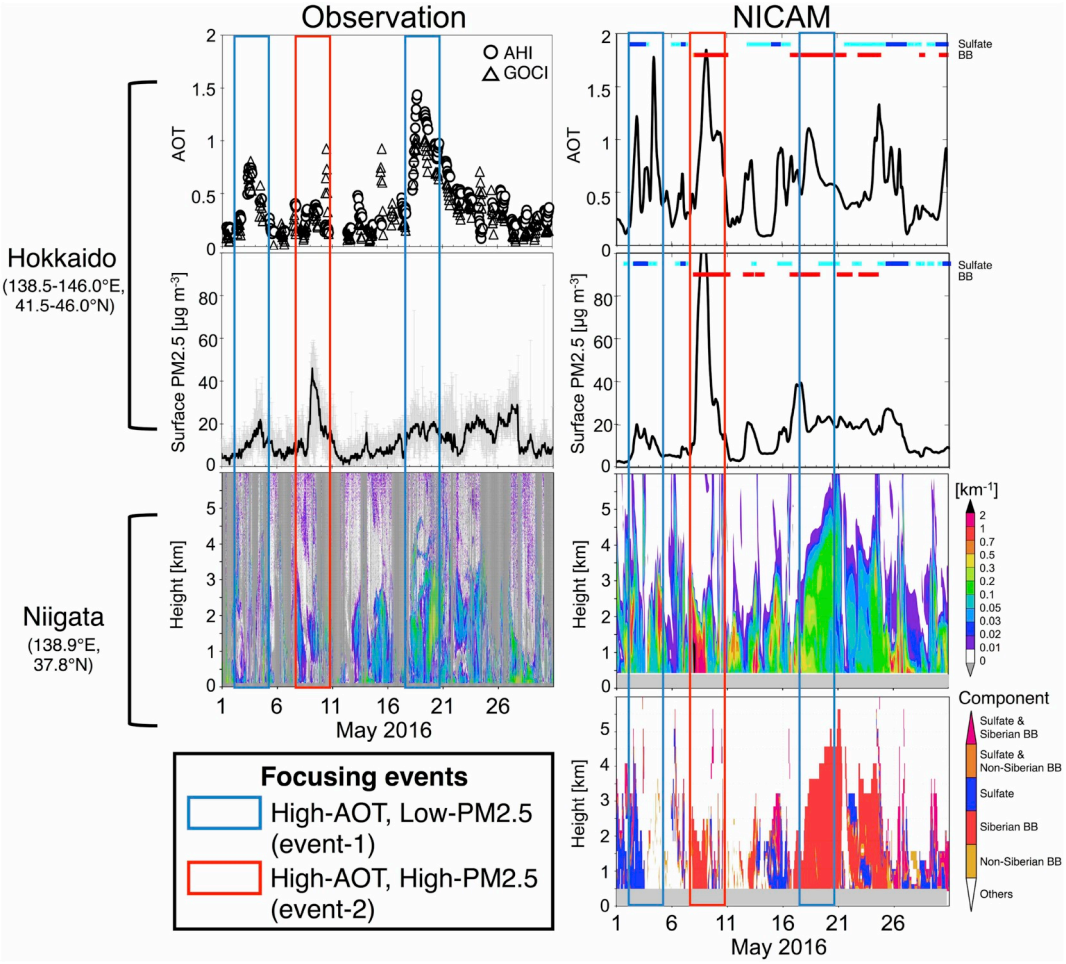

Fig. 8. Hourly variations in the column AOT, surface PM2.5 concentrations, and extinction coefficients for spherical particles according to multiple measurements (left panels) and as simulated by NICAM (right panels) in northern Japan, including Hokkaido (138.5°E–146.0°E, 41.5°N–46.0°N) and Niigata (138.9°E, 37.8°N). The column AOT was retrieved from the AHI and GOCI. The surface PM2.5 concentrations were observed by AEROS at Hokkaido. The extinction coefficients were retrieved from LIDAR. The shaded gray areas in the vertical profiles represent undefined values because of cloud and raindrop contamination and altitude effects. The marks of closed squares in colors around the top in the panels of NICAM-simulated AOT and surface PM2.5 concentrations represent the periods of the high contribution of sulfate in blue (> 30% of the total AOT) and in cyan (> 50% of the total AOT) to the total AOT and those in the high (> 50%) contribution of carbonaceous aerosols in orange (for non-Siberian biomass burning) and in red (for Siberian biomass burning) to the total AOT. The bottom-right panel represents the temporal variation of the major species for the extinction of spherical aerosols obtained by NICAM. The results were defined as those in the high (> 50%) contribution of sulfate to the total extinction and those in the high (> 50%) contribution of carbonaceous aerosols (Siberian biomass burning, BB, and non-Siberian BB) to the total extinction when the total extinction exceeded 0.02 km^{-1}. (For interpretation of the references to colour in this figure legend, the reader is referred to the web version of this article.)

case, which means that high AOT values but low PM2.5 concentrations can indicate either biomass burning or anthropogenic sulfate aerosols.

Fig. 9 is the same as Fig. 8 but for western Japan, especially Fukuoka. According to Fig. 9, three event 2 cases and one event 1 case occurred. On 26–28 May (event 2), the satellite-retrieved AOT reached values close to 1, the observed PM2.5 concentration reached 60 $\mu g\,m^{-3}$, and the LIDAR-retrieved extinction coefficient reached 1 km^{-1}, each of which represented the maximum value (the most polluted air) during May 2016 at Fukuoka. In contrast, the NICAM-simulated AOT and PM2.5 concentrations were comparable to the measured values, but the NICAM-simulated extinction coefficient reached 2 km^{-1}, which was generally the maximum value of the simulation during May 2016 at Fukuoka. On 7–8 May (event 2), the GOCI-retrieved AOT was < 1, the observed PM2.5 concentration was < 40 $\mu g\,m^{-3}$, and the LIDAR-retrieved extinction coefficient was 0.1–0.2 km^{-1} at heights of < 1 km and 3 to 5 km. In contrast, NICAM showed no remarkable peaks in AOT, surface PM2.5 concentrations or vertical extinction. On 13–15 May (event 1), the retrieved AOT was approximately 0.75, which was the second-highest peak in May 2016. The observed PM2.5 concentration was approximately 20 $\mu g\,m^{-3}$, and the LIDAR-retrieved extinction coefficient reached 0.1–0.3 km^{-1}, which were normal values during May 2016. In NICAM, the event 1 case was not particularly remarkable, and the magnitudes of the simulated AOT, PM2.5, and extinction values were comparable to those from the retrievals and measurements. The bottom-right panel obtained by NICAM showed that the major aerosol components of these two event 1 and 2 cases were not from biomass burning but sulfate, and probably a transboundary sulfate. On 22 May (event 2), the major contribution to the total air pollution was Siberian biomass burning. On that day, the GOCI-retrieved AOT was approximately 1, the observed PM2.5 concentration was 20–35 $\mu g\,m^{-3}$, and the LIDAR-retrieved extinction coefficients were 0.5–0.7 km^{-1} at the surface and 0.1–0.2 km^{-1} at heights from the surface up to 2 km. In contrast, the NICAM-simulated AOT was < 0.75, the simulated PM2.5 concentration was 30–35 $\mu g\,m^{-3}$, and the simulated extinction coefficients ranged from 0.1–0.2 km^{-1} at heights from the surface to 2.5 km. NICAM generally reproduced the 3-dimensional structure of the atmospheric aerosols captured by the multiple measurements.

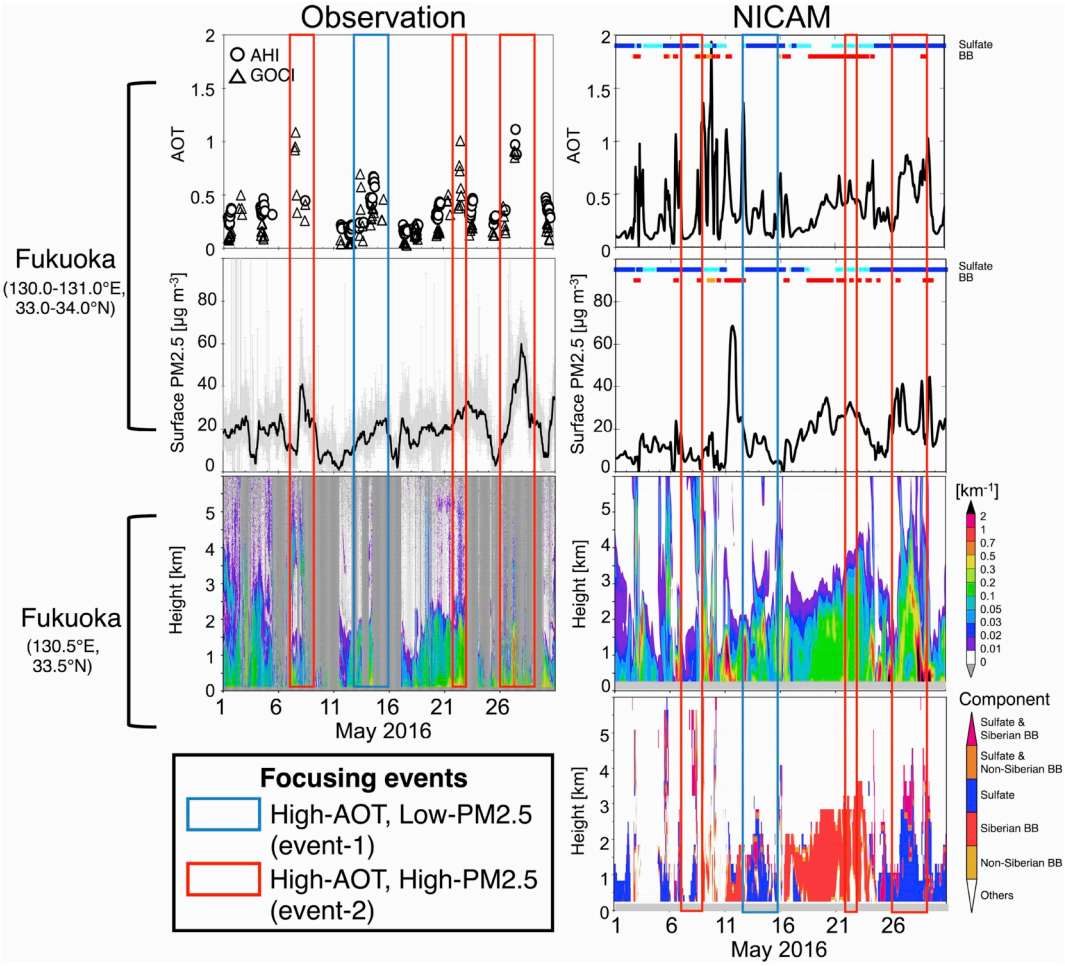

Fig. 9. The same as in Fig. 8, but in western Japan (Fukuoka).

As shown in Fig. 10, three event 1 cases and one event 2 case occurred in Kantou. On 21–26 May (event 2), the satellite-retrieved AOT reached 0.75, the observed PM2.5 concentration reached 35 μg m^{-3}, and the LIDAR-retrieved extinction coefficient was vertically broader at heights from the surface to 3 km, with values of 0.1–0.3 km^{-1}, each of which represented the maximum values during May 2016. The satellite-retrieved AOTs exceeded 0.5 over these 5 days. The NICAM-simulated AOTs were comparable to the observed ones. However, the simulated PM2.5 concentration reached 50 μg m^{-3}, and the simulated extinction coefficient was higher than that from the measurements. The simulated values reached 0.1–0.3 km^{-1} at a height of 4 km, slightly higher than those from the LIDAR results. On 1–3 May (event 1), the retrieved AOT for eastern Japan was the highest in May 2016, with a value above 1. In contrast, the observed PM2.5 concentration was relatively low, with values of approximately 25 μg m^{-3}, and the LIDAR-retrieved extinction coefficient was relatively low, with values of 0.1–0.3 km^{-1} up to a height of 3 km, even though the LIDAR values above 1 km in height were undefined, likely due to clouds. NICAM did not exhibit such strong peaks for the simulated AOT on the same days, but the magnitude was approximately 0.5. The simulated PM2.5 concentrations and simulated extinction were comparable to the measurements, even though the LIDAR values were largely undefined. For the other event 1 case (14–15 May), the behavior of AOT, surface PM2.5 and the vertical profiles of aerosols obtained using multiple measurements were generally similar to those obtained for 1–3 May. The dominant species was sulfate. On 7–8 May (event 1), the satellite-retrieved AOT was < 0.75, the surface PM2.5 concentration was < 25 μg m^{-3}, and the LIDAR-retrieved extinction coefficients were 0.1–0.3 km^{-1} from the surface to heights of 2.5 km. In contrast, the NICAM-simulated AOT was < 1.5, the simulated PM2.5 concentration exceeded 80 μg m^{-3}, and the simulated extinction coefficients ranged from 0.1–0.3 km^{-1} at heights of approximately 2 km. Notably, the simulated surface PM2.5 concentrations and extinction were overestimated compared to the measured results. On these days, the major component of the simulated aerosols was from Siberian biomass burning. From Fig. 10, the major components in the event 1 and 2 cases in eastern Japan were from Siberian biomass burning (only event 2) and anthropogenic sulfate (both events 1 and 2).

In summary, comparisons of the various measurements with model simulations suggest that the event 1 and 2 cases included various compounds and source regions, producing various 4-dimensional structures for the air pollution over Japan. For example, plumes that originated from biomass burning, especially Siberian biomass burning, and anthropogenic sulfate increased the AOT, although the surface PM2.5 concentrations sometimes increased (26–28 May in western Japan and 21–26 May in eastern Japan) or decreased (2–4 and 17–21 May in northern Japan, 13–15 May in western Japan, and 1–3 May in eastern Japan). Therefore, the meteorological conditions, rather than the source region and chemical composition (i.e., biomass burning from Siberia or anthropogenic sulfate from the continent), determined the 4-dimensional structure of the air pollution.

In addition to these specific events, Siberian biomass burning mainly contributed to the air pollution on 11 May (Fukuoka), 16–20 May (Kantou), and 18–24 May (Fukuoka), as indicated in Figs. 8–10. During these days, the simulated AOT generally matched the satellite-retrieved value, whereas the simulated PM2.5 concentrations and extinction were higher than the observed values. As shown in the results

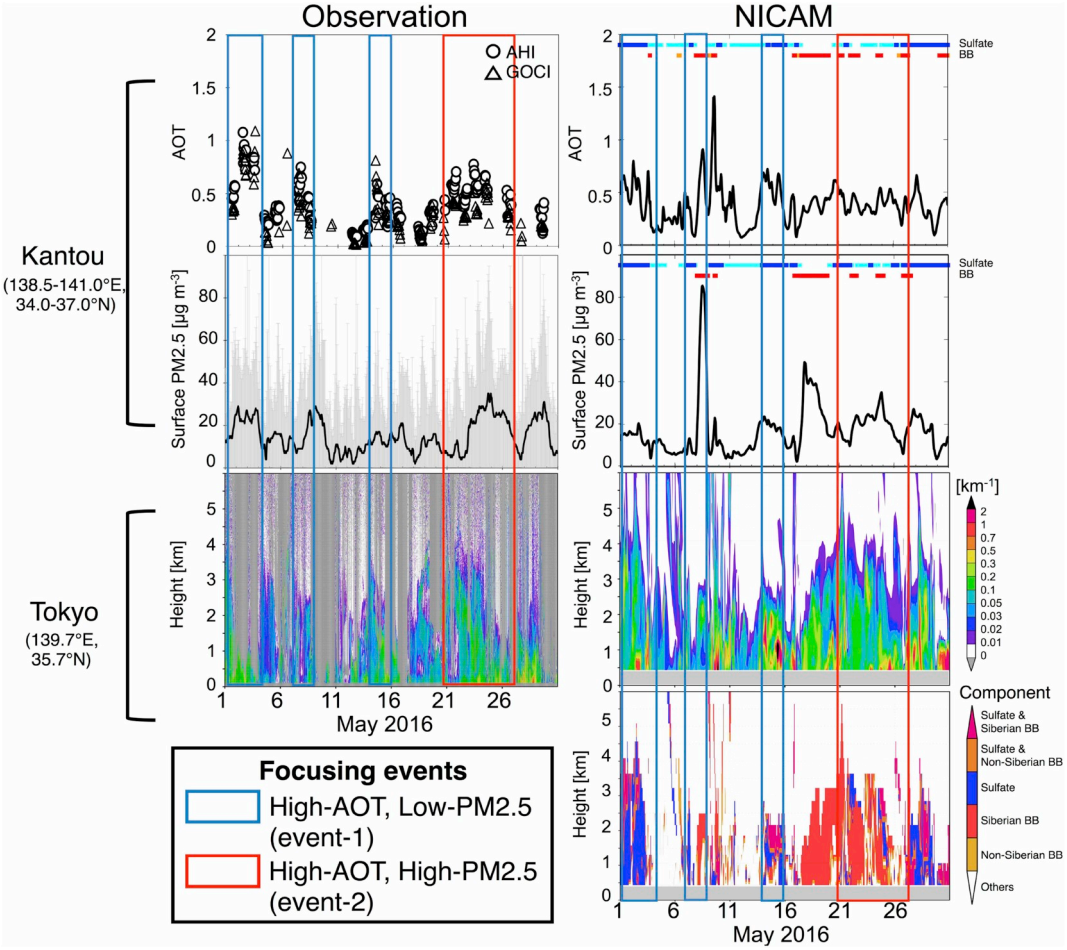

Fig. 10. The same as in Fig. 8, but in eastern Japan (Kantou). The vertical extinction was obtained at Tokyo.

for northern Japan, the simulated extinction coefficient tended to be vertically broader than the observed value. Apart from the air pollution that originated from biomass burning, the 4-dimensional structure of the air pollution that consisted of anthropogenic sulfate was generally captured by a combination of the geostationary satellites and NICAM.

Finally, we summarize this study by showing the monthly and spatially mean values of the aerosols around Japan by using both NICAM and the multiple measured datasets (Fig. 11). Fig. 11 shows the two NICAM results with and without Siberian wildfires by conducting a sensitivity test. In northern Japan, the monthly mean values that were simulated by NICAM with Siberian biomass burning were overestimated compared to those from the measurements. The magnitude relationship of the surface PM2.5 concentrations between the two simulations and the observations was similar to that for the AOT. For NICAM results over northern Japan, the monthly and spatially mean values showed that Siberian biomass burning contributed 0.20 (35%) of AOT and 8.5 $\mu g\,m^{-3}$ (49%) of surface PM2.5 concentrations; these results are overestimated compared to the measurements. The simulated frequency of high (> 50%) contribution of carbonaceous aerosols to total AOT by Siberian biomass burning is 33% in May 2016 (Fig. 8). For surface PM2.5 concentrations, the simulated frequency is 31% in May 2016 (Fig. 8). In the vertical profile, however, the simulation with Siberian biomass burning provided more realistic values at heights of 4–6 km than the simulation without Siberian biomass burning. The relative impacts of the extinction from Siberian biomass burning were estimated to be 38–48% below the 3 km height and 41–66% above the 3 km height.

In western Japan, the monthly and spatially mean AOT and surface PM2.5 concentrations were within the ranges of the observation. The results also showed that Siberian biomass burning contributed approximately 0.03 (7%) of AOT and approximately 4.3 $\mu g\,m^{-3}$ (26%) of surface PM2.5 concentrations. The effects of Siberian biomass burning on the total AOT were small, whereas those on the surface PM2.5 concentrations were not so small. The slight underestimation of both simulated AOT and surface PM2.5 concentrations was likely caused by the underestimation of the simulated aerosols in China and the East China Sea, as mentioned in Fig. 3, due to missing aerosols, e.g., secondary organic aerosols from anthropogenic sources and nitrate in NICAM. The simulated frequency of high (> 50%) contribution of carbonaceous aerosols to total AOT by Siberian biomass burning is 21% in May 2016 (Fig. 9). For surface PM2.5 concentrations, the simulated frequency is also 21% in May 2016 (Fig. 9). In the vertical profile, at the heights below 2 km of the simulated extinction values, even those without Siberian biomass burning were overestimated compared to the LIDAR. Above 3 km in height, the simulated ones were comparable to the LIDAR results. The relative impacts of the extinction from Siberian biomass burning were estimated to be < 16% below 2 km height and 25–41% above 2 km in height.

In eastern Japan, the effects of Siberian biomass burning on the monthly and spatially mean AOT were not as large. The NICAM-simulated AOT with Siberian biomass burning was comparable to the two geostationary satellites. The NICAM-simulated PM2.5 concentrations with Siberian biomass burning were also comparable to the measured values. In NICAM over eastern Japan, the monthly mean values showed that Siberian biomass burning contributed 0.09 (23%) of AOT and 5.4 $\mu g\,m^{-3}$ (32%) of surface PM2.5 concentrations; these results are fully within the range of the observation variability. The simulated frequency of high (> 50%) contribution of carbonaceous aerosols to

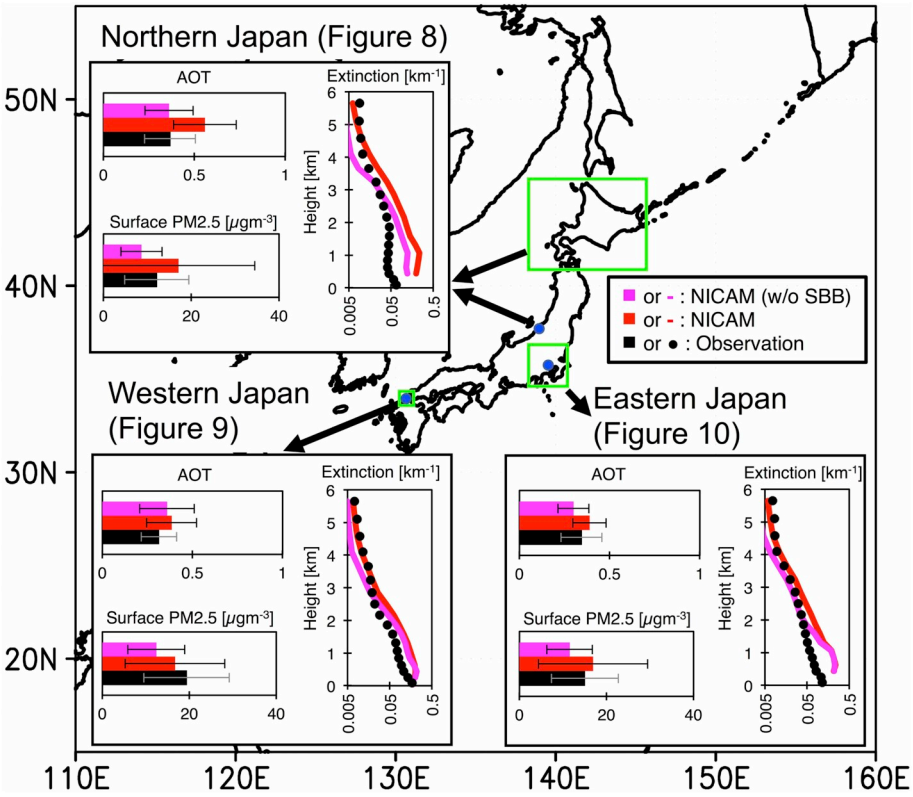

Fig. 11. The monthly and spatially mean values of column AOT, surface PM2.5 concentrations, and extinction coefficients for spherical particles according to multiple measured datasets and as simulated by NICAM in northern, western, and eastern Japan. The observation of AOT was estimated by using all the results from both AHI and GOCI. The colors of red and magenta represent NICAM results with and without Siberian biomass-burning (SBB). The results in black represent observation: multiple geostationary satellites for AOT, AEROS for surface PM2.5 concentrations and LIDAR for the vertical profiles of aerosol extinction. The bars in AOT and surface PM2.5 concentrations show 1-sigma width of the monthly and spatially data. The squares in green represent the spatially averaged area for calculating AOT and surface PM2.5 concentrations. The points in blue represent the location of LIDAR measurements. (For interpretation of the references to colour in this figure legend, the reader is referred to the web version of this article.)

total AOT by Siberian biomass burning is 22% in May 2016 (Fig. 10). For surface PM2.5 concentrations, the simulated frequency is 19% in May 2016 (Fig. 10). The NICAM-simulated extinctions with and without Siberian biomass burning were overestimated at heights below 1.5 km compared to the LIDAR-retrieved values but were comparable to the LIDAR-retrieved values at heights of 3–6 km. The relative impacts of the extinction from Siberian biomass burning were estimated to be < 17% below approximately a 1.5 km height and 36–45% above approximately a 1.5 km height. According to a comparison between northern and western Japan, the NICAM-simulated AOT must be underestimated compared to the satellite-retrieved values, and the NICAM-simulated extinction at heights of 3–6 km must be underestimated compared to the LIDAR-retrieved value. Therefore, a simplified method such as "tuning," which subtracts the aerosols from the biomass burning, would not be a suitable approach to properly reproduce the aerosol distributions from various measurements. This new solution must conduct tuning to improve the vertical distribution of aerosols so that the results are not broadly distributed along the surface. Possible reasons for this enhanced vertical mixing include (1) the larger vertical diffusion that is associated with turbulence and its parameters and (2) the smoothing effects of nudging datasets with coarser resolutions (1° by 1°) compared to the model grid spacing (11 km at the finest resolution). These further developments may be required in the future. These points cannot be solved by a data assimilation of column AOT as proposed by Yumimoto et al. (2016), so these models should be further improved.

5. Conclusions

The objective of this study was to evaluate the spatiotemporal variability of simulated aerosols, including anthropogenic and biomass burning-derived emissions, which are constantly transported from the East Asian continent to the ocean and Japan. The spatial target of our analysis was chosen to be 115°E–155°E, 20°N–50°N, and the temporal target was May 2016. We mainly used the AOT retrieved from two instruments onboard geostationary satellites, the Advanced Himawari Imager (AHI) onboard the geostationary satellite Himawari-8 and the Geostationary Ocean Color Imager (GOCI) onboard the geostationary satellite (COMS), and simulated by NICAM, a semi-regional aerosol-transport model (Goto et al., 2015a).

In this study, we first estimate the accuracies of two geostationary satellites (Himawari-8/AHI and COMS/GOCI) using independent measurements of AERONET and polar-orbiting satellites, MODIS/Terra and MODIS/Aqua. The AHI can be used to estimate the AOT over a wide area with unprecedentedly high temporal resolution around East Asia. The GOCI can also be used to estimate the AOT, but over a relatively limited area in East Asia (116°E-146°E, 24°N-48°N). We found that the bias between MODIS and AERONET tended to be larger than that between the two geostationary satellites and AERONET. The correlation coefficients between geo-stationary satellites and AERONET are generally high to moderate, so that the satellite results can be used as reference data for model evaluation. We used the data retrieved independently from these two geostationary satellites to take into account the observational uncertainty. In situ sampling, such as from the AEROS installation over Japan, ground-based remote-sensing measurements (such as LIDAR), and polar-orbiting satellite sensors (such as MODIS) have limited spatial and temporal coverage, so geostationary satellites such as Himawari-8 and COMS can obtain aerosol information with greater spatial coverage and higher temporal resolution, allowing these satellites to be more powerful than other measurements.

After this demonstration of the availability of two geostationary satellites as reference datasets, we investigated the differences in the AOT as shown by AHI, GOCI, MODIS and NICAM for the NICAM evaluation. A comparison of the AOT at 00:00 UTC (09:00 JST) on 18 May 2016 with both the AHI and GOCI retrievals indicated that the AHI, GOCI, and NICAM captured a high-AOT plume over the northern Sea of Japan. Furthermore, the detailed horizontal distributions of the high-AOT plume as simulated by NICAM were relatively consistent with those from the AHI and GOCI. On the chosen day, the AHI and GOCI clearly detected the transport of this high-AOT plume over Hokkaido

(northern Japan). Currently, no other measurements have captured such a detailed horizontal distribution of the plume as have the AHI and GOCI onboard geostationary satellites, as shown in Fig. 2. The temporal evolution of the aerosols simulated by NICAM generally matched the results from the AHI, GOCI and MODIS.

The monthly means of the AHI-retrieved, GOCI-retrieved and NICAM-simulated AOT were 0.36, 0.30 (GOCI can only cover the area from 116°E–146°E and 24°N–48°N) and 0.34 (0.33 in NICAM, considering the spatiotemporal collocation with GOCI), respectively. The correlation between the AHI and NICAM was moderate, with a correlation coefficient of 0.39 (significant level of 0.05), whereas the correlation coefficient for the GOCI and NICAM was lower, with a value of 0.26 (significant level of 0.05). In this study, the difference in AOT between AHI and GOCI is assumed to be an observational error. A comparison of the spatiotemporal variations in the AOT showed that the model generally captured the transport of aerosols over Japan in May 2016. The correlation coefficient between AHI and NICAM was > 0.4 (significant level of 0.05) in 42% of the target area (115°E–155°E, 20°N–50°N), the NMB was within 20% in 46% of the target area, and the RMSE was < 0.2 in 37% of the target area. The statistical metrics are generally similar for the comparison between the GOCI and NICAM. Therefore, we conclude that NICAM could generally reproduce the satellite-retrieved AOT based on a comparison between the mean and correlation coefficient (which are often used in model evaluation). In the areas where the NMB and RMSE were relatively larger, the NICAM-simulated AOTs were larger than both the AHI-retrieved and GOCI-retrieved values, or the correlation coefficients were negative; some examples are in the Sea of Japan and the ocean around western Japan. The PDF of the AHI-retrieved AOT produced +2.07 skewness and 9.16 kurtosis, whereas the PDF of the NICAM-simulated AOT produced +6.00 skewness and 91.24 kurtosis. These differences in the skewness and kurtosis in the PDF between the AHI and NICAM are similar to those obtained for the GOCI and NICAM. In Fig. 4, these two values exhibited narrower distributions in the PDF from NICAM compared to those from the geostationary satellites. However, the differences in the AOT between the geostationary satellites and NICAM were relatively low, because the AOT from Siberian biomass burning over the Sea of Japan was overestimated, and the AOT from anthropogenic sulfate in eastern China and western Japan, as well as the partially background aerosols the over the remote ocean, was underestimated. These values canceled out when calculating the monthly average values. The low correlation coefficient between NICAM and geostationary satellites can be caused by slight differences in the timing of high AOT between NICAM and satellites, as well as slight differences in the meteorological fields between NICAM (perhaps the reanalysis data) and the real atmosphere.

After comparing the AHI-retrieved, GOCI-retrieved, and NICAM-simulated AOT, we assessed how well the geostationary satellite data, surface PM2.5 measurements, LIDAR data, and the model reproduced the 4-dimensional structure of transboundary pollution, including biomass burning during May 2016. A combined analysis of these observations, i.e., column AOT, surface PM2.5 concentrations, and vertical profile of the extinction coefficient, and the NICAM simulations with and without Siberian biomass burning emissions indicated that the 4-dimensional structures of the transboundary air pollution depended not on the source region and chemical composition but on the meteorological conditions. For example, plumes, including high AOT from biomass burning, are sometimes transported to the surface and directly affect the surface PM2.5 concentrations. Other plumes, which are often produced by biomass burning, exhibit low surface PM2.5 concentrations but high column AOT values, indicating that the plume is transported at high altitudes and does not reach the ground. The model successfully reproduced the behavior of anthropogenic sulfate but did not adequately reproduce the aerosol vertical distribution from biomass burning around Japan.

We also discussed the effects of the biomass burning that occurred in May 2016 on the aerosol levels around Japan by conducting a sensitivity test for Siberian biomass burning with NICAM. Biomass burning from Siberian forest fires strongly influenced the aerosol levels in May 2016 over Japan. Although previous studies, such as those of Ikeda and Tanimoto (2015), have noted the effects of Siberian biomass burning on northern Japan, this study suggested that Siberian biomass burning affects air quality throughout the country, including western and eastern Japan, especially above the 3–6 km height. At the heights, the relative impacts of the extinction from Siberian biomass burning were estimated to be 41–66% (northern Japan), 25–41% (western Japan) and 37–44% (eastern Japan). In the column amount, i.e., AOT, Siberian biomass burning contributed 0.20 or 35% (northern Japan), 0.03 or 7% (western Japan) and 0.09 or 23% (Eastern Japan), respectively. In the surface concentrations, i.e., the monthly and spatially mean surface PM2.5 concentrations, Siberian biomass burning contributed $8.5\,\mu g\,m^{-3}$ or 49% (northern Japan), $4.3\,\mu g\,m^{-3}$ or 26% (western Japan) and $5.4\,\mu g\,m^{-3}$ or 32% (eastern Japan). Because simulations can estimate only the spatiotemporal variability of the aerosol chemical components over larger areas, properly predicting such strong events is critical to understanding the 4-dimensional structure of air pollution. Therefore, aerosol simulations, especially of vertical profiles, must be improved.

Acknowledgments and data

Data used to support this article can be obtained by request to the corresponding author (goto.daisuke@nies.go.jp). We acknowledge the developers and administrators of NICAM (http://nicam.jp/), SPRINT-ARS (https://sprintars.riam.kyushu-u.ac.jp/indexe.html), NIES-LIDAR (acquired by contacting nsugimot@nies.go.jp and shimizua@nies.go.jp), AHI (http://www.eorc.jaxa.jp/ptree/index.html), GOCI (http://kosc.kiost.ac.kr/), MODIS (https://modis.gsfc.nasa.gov/) and the relevant PIs of the AERONET sites (https://aeronet.gsfc.nasa.gov/). The CAMS Global Fire Assimilation System (GFAS) inventory was provided by ECMWF (http://apps.ecmwf.int/datasets/data/cams-gfas/), which was accessed on 12 March 2018. The PM2.5 surface measurements (http://soramame.taiki.go.jp/) are provided by local government measurements under the operation of the Ministry of the Environment, Japan (MOEJ). The National Centers for Environmental Prediction (NCEP) FNL Operational Model Global Tropospheric Analyses were provided by NCEP, National Weather Service, NOAA, and the U.S. Department of Commerce (2000) (https://rda.ucar.edu/datasets/ds083.2/), which was accessed on 22 March 2018. The back trajectories used in Fig. 2 were calculated by the NOAA HYSPLIT trajectory model (https://www.ready.noaa.gov/HYSPLIT.php), which was accessed on 17 October 2018. Some of the authors were supported by the Global Environment Research and Technology Development Fund S-12 of MOEJ, the Japan Aerospace Exploration Agency (JAXA)/Earth Observation Priority Research, and the Grant-in-Aid for Young Scientist B (grant 26740010) and A (grant 17H04711). Additionally, some of the authors were supported by the following projects: National Institute for Environmental Studies, Japan (NIES), and MOEJ GOSAT2, JAXA/EarthCARE, JAXA/GCOM-C, and the Japan Science and Technology (JST), CREST/EMS/TEEDDA. Some of the authors were supported by the National Strategic Project-Fine particle of the National Research Foundation of Korea (NRF) funded by the Ministry of Science and ICT, the Ministry of Environment, and the Ministry of Health and Welfare (NRF-2017M3D8A1092021) in Korea. Development of the integrated data processing system for GOCI-II" funded by the Ministry of Ocean and Fisheries, Korea. The model simulations were performed by using the supercomputer resources JAXA/JSS2, NIES/NEC SX-ACE, K computer (150156, 160004, 170017 and 180012), and PRIMEHPC FX10 (University of Tokyo, Japan). We thank Tran Thi Ngoc Trieu for help in processing the nudging datasets.

References

Choi, J.K., Park, Y.J., Ahn, J.H., Lim, H.S., Eom, J., Ryu, J.H., 2012. GOCI, the world's first geostationary ocean color observation satellite, for the monitoring of temporal variability in coastal water turbidity. J. Geophys. Res. Oceans 117. https://doi.org/10.1029/2012jc008046.

Choi, M., Kim, J., Lee, J., Kim, M., Park, Y.-J., Jeong, U., Kim, W., Hong, H., Holben, B., Eck, T.F., Song, C.H., Lim, J.-H., Song, C.-K., 2016. GOCI Yonsei Aerosol Retrieval (YAER) algorithm and validation during the DRAGON-NE Asia 2012 campaign. Atmos Meas. Tech. 9 (3), 1377–1398. https://doi.org/10.5194/amt-9-1377-2016.

Choi, M., Kim, J., Lee, J., Kim, M., Park, Y.-J., Holben, B., Eck, T.F., Li, Z., Song, C.H., 2018. GOCI Yonsei aerosol retrieval version 2 aerosol products: an improved algorithm description and error analysis with uncertainty estimation from 5-year validation over East Asia. Atmos. Meas. Tech. 11, 385–408. https://doi.org/10.5194/amt-11-385-2018.

Dai, T., Schutgens, N.A.J., Goto, D., Shi, G., Nakajima, T., 2014. Improvement of aerosol optical properties modeling over Eastern Asia with MODIS AOD assimilation in a global non-hydrostatic icosahedral aerosol transport model. Environ. Pollut. 195, 319–329. https://doi.org/10.1016/j.envpol.2014.06.021.

Fukuda, S., Nakajima, T., Takenaka, H., Higurashi, A., Kikuchi, N., Nakajima, T.Y., Ishida, H., 2013. New approaches to removing cloud shadows and evaluating the 380 nm surface reflectance for improved aerosol optical thickness retrievals from the GOSAT/TANSO - Cloud and Aerosol Imager. J. Geophys. Res. Atmos. 118, 13–520.

Goto, D., Dai, T., Satoh, M., Tomita, H., Uchida, J., Misawa, S., Inoue, T., Tsuruta, H., Ueda, K., Ng, C.F.S., Takami, A., Sugimoto, N., Shimizu, A., Ohara, T., Nakajima, T., 2015a. Application of a global nonhydrostatic model with a stretched-grid system to regional aerosol simulations around Japan. Geosci. Model Dev. 8, 235–259. https://doi.org/10.5194/gmd-8-235-2015.

Goto, D., Nakajima, T., Dai, T., Takemura, T., Kajino, M., Matsui, H., Takami, A., Hatakeyama, S., Sugimoto, N., Shimizu, A., Ohara, T., 2015b. An evaluation of simulated particulate sulfate over East Asia through global model intercomparison. J. Geophys. Res. Atmos. 120, 6247–6270. https://doi.org/10.1002/2014JD021693.

Goto, D., Ueda, K., Ng, C.F.S., Takami, A., Ariga, T., Matsuhashi, K., Nakajima, T., 2016. Estimation of excess mortality due to long-term exposure to PM2.5 in Japan using a high-resolution model for present and future scenarios. Atmos. Environ. 140, 320–332. https://doi.org/10.1016/j.atmosenv.2016.06.015.

Goto, D., Nakajima, T., Dai, T., Yashiro, H., Sato, Y., Suzuki, K., Uchida, J., Misawa, S., Yonemoto, R., Trieu, T.T.N., Tomita, H., Satoh, M., 2018. Multi-Scale simulations of atmospheric pollutants using a non-hydrostatic icosahedral atmospheric model. In: Vadrevu, K., Ohara, T., Justice, C. (Eds.), Land-Atmospheric Research Applications in South and Southeast Asia. Springer Remote Sensing/Photogrammetry. Springer, Cham.

Hara, Y., Uno, I., Shimizu, A., Matsui, I., Yumimoto, K., Kurokawa, J., Ohara, T., Liu, Z., 2011. Seasonal characteristics of spherical aerosol distribution in Eastern Asia: integrated analysis using ground/space-based lidars and a chemical transport model. SOLA 7, 121–124. https://doi.org/10.2151/sola.2011-031.

Higurashi, A., Nakajima, T., 1836. Detection of aerosol types over the East China Sea near Japan from four-channel satellite data. Geopys. Res. Lett. 29. https://doi.org/10.1029/2002GL015357.

Holben, B.N., Eck, T.F., Slutsker, I., Tanré, D., Buis, J.P., Setzer, A., Vermote, E., Reagan, J.A., Kaufman, Y., Nakajima, T., Lavenu, F., Jankowiak, I., Smirnov, A., 1998. AERONET - a federated instrument network and data archive for aerosol characterization. Remote Sens. Environ. 66, 1–16.

Holben, B.N., Kim, J., Sano, I., Mukai, S., Eck, T.F., Giles, D.M., Schafer, J.S., Sinyuk, A., Slutsker, I., Smirnov, A., Sorokin, M., Anderson, B.E., Che, H., Choi, M., Crawford, J.H., Ferrare, R.A., Garay, M.J., Jeong, U., Kim, M., Kim, W., Knox, N., Li, Z., Lim, H.S., Liu, Y., Maring, H., Nakata, M., Pickering, K.E., Piketh, S., Redemann, J., Reid, J.S., Salinas, S., Seo, S., Tan, F., Tripathi, S.N., Toon, O.B., Xiao, Q., 2018. An overview of mesoscale aerosol processes, comparisons, and validation studies from DRAGON networks. Atmos. Chem. Phys. 18, 655–671. https://doi.org/10.5194/acp-18-655-2018.

Hsu, N.C., Jeong, M.J., Bettenhausen, C., Sayer, A.M., Hansell, R., Seftor, C.S., Huang, J., Tsay, S.C., 2013. Enhanced Deep Blue aerosol retrieval algorithm: the second generation. J. Geophys. Res.-Atmos. 118, 9296–9315.

Hu, J., Wang, P., Ying, Q., Zhang, H., Chen, J., Ge, X., Li, X., Jiang, J., Wang, S., Zhang, J., Zhao, Y., Zhang, Y., 2017. Modeling biogenic and anthropogenic secondary organic aerosol in China. Atmos. Chem. Phys. 17, 77–92. https://doi.org/10.5194/acp-17-77-2017.

Ikeda, K., Tanimoto, H., 2015. Exceedances of air quality standard level of $PM_{2.5}$ in Japan caused by Siberian wildfires. Environ. Res. Lett. 10, 105001. https://doi.org/10.1088/1748-9326/10/10/105001.

Kaiser, J.W., Heil, A., Andreae, M.O., Benedetti, A., Chubarova, N., Jones, L., Morcrette, J.-J., Razinger, M., Schultz, M.G., Suttie, M., van der Werf, G.R., 2012. Biomass burning emissions estimated with a global fire assimilation system based on observed fire radiative power. Biogeosciences 9, 527–554.

Kaufman, Y.J., Tanre, D., Remer, L.A., Vermote, E.F., Chu, A., Holben, B.N., 1997. Operational remote sensing of tropo- spheric aerosol over land from EOS moderate resolution imaging spectroradiometer. J. Geophys. Res.-Atmos. 102, 17051–17067.

Kikuchi, M., Murakami, H., Suzuki, K., Nagao, T.M., Higurashi, A., 2018. Improved Hourly estimates of Aerosol Optical Thickness using Spatiotemporal Variability Derived from Himawari-8 Geostationary Satellite. IEEE Trans. Geosci. Remote Sens. 56 (6), 3442–3455. https://doi.org/10.1109/TGRS.2018.2800060.

Kinne, S., Lohmann, U., Feichter, J., Timmreck, C., Schulz, M., Ghan, S., Easter, R., Chin, M., Ginoux, P., Takemura, T., Tegen, I., Koch, D., Herzog, M., Penner, J., Pitari, G., Holben, B., Eck, T., Smirnov, A., Dubovik, O., Slutsker, I., Tanré, D., Torres, O., Mishchenko, M., Geogdzhayev, I., Chu, D.A., Kaufman, Y., 2003. Monthly averages of aerosol properties: a Global comparison among models, satellite data and AERONET ground data. J. Geophys. Res. 108, 4634.

Lee, J., Kim, J., Song, C.H., Ryu, J.H., Ahn, Y.H., Song, C.K., 2010. Algorithm for retrieval of aerosol optical properties over the ocean from the Geostationary Ocean Color Imager. Remote Sens. Environ. 114, 1077–1088.

Levy, R.C., Mattoo, S., Munchak, L.A., Remer, L.A., Sayer, A.M., Patadia, F., Hsu, N.C., 2013. The Collection 6 MODIS aerosol products over land and ocean. Atmos. Meas. Tech. 6, 2989–3034. https://doi.org/10.5194/amt-6-2989-2013.

Mellor, G.L., Yamada, T., 1974. A Hierarchy of Turbulence Closure Models for Planetary Boundary Layers. J. Atmos. Sci. 31, 1791–1806.

Morino, Y., Nagashima, T., Sugata, S., Sato, K., Tanabe, K., Noguchi, T., Takami, A., Tanimoto, H., Ohara, T., 2015. Verification of chemical transport models for PM2.5 chemical composition using simultaneous measurement data over Japan. Aerosol Air Qual. Res. 15, 2009–2023. https://doi.org/10.1029/aaqr.2015.02.0120.

Nakajima, T., Yoon, S.-C., Ramanathan, V., Shi, G.-Y., Takemura, T., Higurashi, A., Takamura, T., Aoki, K., Sohn, B.-J., Kim, S.-W., Tsuruta, H., Sugimoto, N., Shimizu, A., Tanimoto, H., Sawa, Y., Lin, N.-H., Lee, C.-T., Goto, D., Schutgens, N., 2007. Overview of the atmospheric brown cloud East Asian Regional Experiment 2005 and a study of the aerosol direct radiative forcing in East Asia. J. Geophys. Res. 112, D24S91. https://doi.org/10.1029/2007JD009009.

Nakanishi, M., Niino, H., 2004. An improved Mellor–Yamada level 3 model with condensation physics: its design and verification. Bound.-Layer Meteorol. 112, 1–31. https://doi.org/10.1023/B:BOUN.0000020164.04146.98.

Park, R.S., Song, C.H., Han, K.M., Park, M.E., Lee, S.-S., Kim, S.-B., Shimizu, A., 2011. A study on the aerosol optical properties over East Asia using a combination of CMAQ-simulated aerosol optical properties and remote-sensing data via a data assimilation technique. Atmos. Chem. Phys. 11, 12275–12296. https://doi.org/10.5194/acp-11-12275-2011.

Rolph, G., Stein, A., Stunder, B., 2017. Real-time environmental applications and display system: READY. Environ. Model Softw. 95, 210–228. https://doi.org/10.1016/j.envsoft.2017.06.025.

Sato, T., Miura, H., Satoh, M., Takayabu, Y.N., Wang, Y., 2009. Diurnal cycle of precipitation in the tropics simulated in a global cloud-resolving model. J. Clim. 22, 4809–4826. https://doi.org/10.1175/2009JCLI2890.1.

Satoh, M., Matsuno, T., Tomita, H., Miura, H., Nasuno, T., Iga, S., 2008. Nonhydrostatic icosahedral atmospheric model (NICAM) for global cloud resolving simulations. J. Comput. Phys. 227, 3486–3514. https://doi.org/10.1016/j.jcp.2007.02.006.

Satoh, M., Inoue, T., Miura, H., 2010. Evaluations of cloud properties of global and local cloud system resolving models using CALIPSO and CloudSat simulators. J. Geophys. Res. 115, D00H14. https://doi.org/10.1029/2009JD012247.

Satoh, M., Tomita, H., Yashiro, H., Miura, H., Kodama, C., Seiki, T., Noda, A.T., Yamada, Y., Goto, D., Sawada, M., Miyoshi, T., Niwa, Y., Hara, M., Ohno, T., Iga, S., Arakawa, T., Inoue, T., Kubokawa, H., 2014. The non-hydrostatic icosahedral atmospheric model: description and development. Prog. Earth Planetary Sci. 1, 18–49. https://doi.org/10.1186/s40645-014-0018-1.

Sayer, A.M., Munchak, L.A., Hsu, N.C., Levy, R.C., Bettenhausen, C., Jeong, M.-J., 2014. MODIS collection 6 aerosol products: comparison between aqua's e-deep blue, dark target, and "merged" data sets, and usage recommendations. J. Geophys. Res.-Atmos. 119, 13965–13989.

Schutgens, N.A.J., Partridge, D.G., Stier, P., 2016. The importance of temporal collocation for the evaluation of aerosol models with observations. Atmos. Chem. Phys. 16, 1065–1079. https://doi.org/10.5194/acp-16-1065-2016.

Seiki, T., Satoh, M., Tomita, T., Nakajima, T., 2014. Simultaneous evaluation of ice cloud microphysics and nonsphericity of the cloud optical properties using hydrometeor video sonde and radiometer sonde in situ observations. J. Geophys. Res. 119, 6681–6701. https://doi.org/10.1002/2013JD021086.

Seinfeld, J.H., Carmichael, G.R., Arimoto, R., Conant, W.C., Brechtel, F., Bates, T.S., Cahill, T.A., Clarke, A.D., Doherty, S.J., Flatau, P.J., Huebert, B.J., Kim, J.Y., Markowicz, M., Quinn, P.K., Russell, L.M., Russell, P.B., Shimizu, A., Shinozuka, Y., Song, C.H., Tang, Y., Uno, I., Vogelmann, A.M., Weber, R.J., Woo, J.-H., Zhang, X.Y., 2004. Regional climatic and atmospheric chemical effects of Asian dust and pollution. Bull. Am. Meterol. Soc. 85 (3), 367–380. https://doi.org/10.1175/BAMS-85-3-367.

Shimizu, A., Sugimoto, N., Matsui, I., Arao, K., Uno, I., Murayama, T., Kagawa, N., Aoki, K., Uchiyama, A., Yamazaki, A., 2004. Continuous observations of Asian dust and other aerosols by polarization lidars in China and Japan during ACE-Asia. J. Geophys. Res. 109, D19S17. https://doi.org/10.1029/2002JD003253.

Stein, A.F., Draxler, R.R., Rolph, G.D., Stunder, B.J.B., Cohen, M.D., Ngan, F., 2015. NOAA' HYSPLIT atmospheric transport and dispersion modeling system. Bull. Amer. Meteor. Soc. 96, 2059–2077. https://doi.org/10.1175/BAMS-D-14-00110.1.

Sugimoto, N., Uno, I., Nishikawa, M., Shimizu, A., Matsui, I., Dong, X., Chen, Y., Quan, H., 2003. Record heavy Asian dust in Beijing in 2002: observations and model Analysis of recent events. Geophys. Res. Lett. 30 (12), 1640 (doi:10.1029/2002GL016349).

Sugimoto, N., Matsui, I., Shimizu, A., Nishizawa, T., Hara, T., Xie, C., Uno, I., Yumimoto, K., Wang, Z., Yoon, S.-C., 2008. Lidar network observations of tropospheric aerosols. Proc. SPIE 7153https://doi.org/10.1117/12.806540. 71530A–71530A–13.

Suzuki, K., Nakajima, T., Satoh, M., Tomita, H., Takemura, T., Nakajima, T.Y., Stephens, G.L., 2008. Global cloud-system-resolving simulation of aerosol effect on warm clouds. Geophys. Res. Lett. 35, L19817. https://doi.org/10.1029/2008GL035449.

Takemura, T., Nozawa, T., Emori, S., Nakajima, T.Y., Nakajima, T., 2005. Simulation of climate response to aerosol direct and indirect effects with aerosol transport-radiation model. J. Geophys. Res. 110, D02202. https://doi.org/10.1029/2004JD005029.

Tomita, H., 2008a. A stretched grid on a sphere by new grid transformation. J. Meteorol. Soc. Jpn. 86A, 107–119.

Tomita, H., 2008b. New microphysics with five and six categories with diagnostic generation of cloud ice. J. Meteorol. Soc. Jpn. 86A, 121–142.

Tomita, H., Satoh, M., 2004. A new dynamical framework of nonhydrostatic global model using the icosahedral grid. Fluid Dyn. Res. 34, 357–400.

Tomita, H., Miura, H., Iga, S., Nasuno, T., Satoh, M., 2005. A global cloud-resolving simulation: preliminary results from an aqua planet experiment. Geophys. Res. Lett. 32, L08805 (doi:10.1029/2005GL022459).

Toth, T.D., Zhang, J., Campbell, J.R., Reid, J.S., Shi, Y., Johnson, R.S., Smirnov, A., Vaughan, M.A., Winker, D.M., 2013. Investigating enhanced Aqua MODIS aerosol optical depth retrievals over the mid-to-high latitude Southern Oceans through intercomparision with co-located CALIOP, MAN, and AERONET data sets. J. Geophys. Res. Atmos. 118 (10). https://doi.org/10.1002/jgrd.50311.

Trieu, T., Goto, D., Yashiro, H., Murata, R., Sudo, K., Tomita, H., Satoh, M., Nakajima, T., 2017. Evaluation of summertime surface ozone in Kanto area of Japan using a semi-regional model and observation. Atmos. Environ. 153, 163–181. https://doi.org/10.1016/j.atmosenv.2017.01.030.

Yasunari, T.J., Kim, K.-M., da Silva, A.M., Hayasaki, M., Akiyama, M., Murao, N., 2018. Extreme air pollution events in Hokkaido, Japan, traced back to early snowmelt and large-scale wildfires over East Eurasia: Case studies. Sci. Rep. 8, 6413. https://doi.org/10.1038/s41598-018-24335-w.

Yoshida, M., Kikuchi, M., Nagao, T.M., Murakami, H., Nomaki, T., Higurashi, A., 2018. Common retrieval of atmospheric aerosol properties for imaging satellite sensors. J. Meteorol. Soc. Jpn. 96B, 193–209. https://doi.org/10.2151/jmsj.2018-039.

Yumimoto, K., Nagao, T.M., Kikuchi, M., Sekiyama, T.T., Murakami, H., Tanaka, T.Y., Ogi, A., Irie, H., Khatri, P., Okumura, H., Arai, K., Morino, I., Uchino, O., Maki, T., 2016. Aerosol data assimilation using data from Himawari-8, a next-generation geostationary meteorological satellite. Geophys. Res. Lett. 43, 5886–5894. https://doi.org/10.1002/2016GL069298.

Yumimoto, K., Tanaka, T.Y., Yoshida, M., Kikuchi, M., Nagao, T.M., Murakami, H., Maki, T., 2018. Assimilation and forecasting experiment for heavy Siberian wildfire smoke in May 2016 with Himawari-8 aerosol optical thickness. J. Meteorol. Soc. Jpn. 96B, 133–149. https://doi.org/10.2151/jmsj.2018-035.